

Dynamic restrengthening and stress heterogeneity explain megathrust earthquake complexity

Jeremy Wing Ching Wong,^{1*} Alice-Agnes Gabriel,^{1,2} Wenyuan Fan¹

¹Institute of Geophysics and Planetary Physics, Scripps Institution of Oceanography
University of California, San Diego, CA, USA

²Department of Earth and Environmental Sciences,
Ludwig-Maximilians-Universität München, Munich, Germany

*E-mail: jeremywong@ucsd.edu

May 15, 2025

This manuscript is an ArXiv preprint and has been submitted for possible publication in a peer reviewed journal. Please note that this has not been peer reviewed before and is currently undering peer review for the first time. Subsequent versions of this manuscript may have slightly different content.

Abstract

Megathrusts host Earth’s largest earthquakes. Understanding the physical conditions controlling their rupture dynamics is critical for assessing seismic and tsunami hazards. These earthquakes often display complex rupture dynamics, exemplified by the 2011 Tohoku-Oki earthquake, which exhibited multiple rupture episodes, depth-dependent seismic radiation, and substantial tsunamigenic slip near the trench. However, whether such complexity arises from pre-existing physical conditions remains uncertain. Here, we demonstrate that the observed rupture complexity of the Tohoku-Oki earthquake can spontaneously and self-consistently emerge, driven by rapid coseismic frictional restrengthening and data-informed initial stress heterogeneity, without prescribing frictional asperities. We use an ensemble of 3D dynamic rupture simulations to identify that mixed downdip pulse-like and updip crack-like rupture are driven by dynamic stress redistribution with episodic rupture reactivation. By featuring low fault strength compared to its dynamic stress drop, a preferred model can consistently reproduce the observed complex depth-dependent propagation speeds, multiple rupture fronts as imaged by back-projection, and large tsunamigenic slip at the trench. Our findings demonstrate that preexisting stress heterogeneity conjointly with dynamic frictional weakening and restrengthening drives seemingly unexpected megathrust rupture complexity, highlighting the need to include dynamic effects into physics-based seismic and tsunami hazard assessments of future earthquakes.

Introduction

Large megathrust earthquakes propagate rapidly, rupture over hundreds of kilometers within minutes, generate strong ground shaking, and, in certain instances, cause devastating tsunamis. These seismic and tsunami hazards are directly controlled by rupture dynamics and shallow fault slip behavior [1, 2]. The 2011 M_W 9.0 Tohoku-Oki earthquake, one of the most destructive earthquakes of the 21st century, exhibited unexpected complexities throughout its rupture process: possible reactivation at the hypocenter [3–5], depth-dependent seismic radiation [6, 7], large slip to the trench exceeding 50–60 m [8, 9], and an unusually limited along-strike rupture extent for its magnitude [2]. This event demonstrates that the physical mechanisms controlling devastating earthquake rupture dynamics remain poorly understood, limiting accurate hazard assessment for future megathrust earthquakes, such as in the Pacific Northwest, Nankai Trough, and New Zealand [10, 11].

Although the 2011 Tohoku-Oki earthquake is among the best-recorded megathrust events, the physical mechanisms underlying its complexity remain debated [2], and its slip models show significant variability [12]. Previous studies attribute some of this event’s complexities to preexisting stress or frictional-strength fault asperities (e.g., [13–15]). However, the interplay between preexisting fault conditions and dynamically evolving rupture processes as drivers of earthquake complexity, as well as their distinct observational signatures, remains incompletely resolved. Here, we show that the surprising characteristics of the Tohoku-Oki earthquake arise dynamically during rupture evolution.

The frictional properties of fault rocks and gouges govern fault strength and slip. Thus, a key factor in earthquake dynamics is the frictional response to rupture velocity changes, which controls nucleation, propagation, and arrest [16–18]. Rate-and-state friction laws effectively describe fault friction at interseismic to slow slip rates, capturing the dependence of friction on sliding velocity and state evolution [19, 20]. Laboratory and theoretical studies show that at coseismic slip rates, fault friction likely exhibits even stronger velocity weakening, followed by equally rapid frictional healing as slip rates decrease [21–23]. Such rapid dynamic friction evolution generates complex faulting behavior, facilitating diverse earthquake rupture styles and speeds, slip reactivation, and multi-fault interaction in laboratory experiments and numerical simulations [24–27].

Stress heterogeneity can spontaneously develop from slow and fast fault slip, even under spatially uniform frictional conditions [28–30]. While frictional heterogeneity likely arises from static factors, such as depth, temperature, and lithology, this alone may not explain complex and variable slip behavior [1]. In distinction, stress heterogeneity is expected to be ubiquitous and dynamically evolving throughout the seismic cycle. While inherent observational limitations preclude directly observing fault strength heterogeneity, we here demonstrate that integrating rapid frictional fault weakening and restrengthening with observationally informed stress heterogeneity explains key rupture characteristics of the 2011 Tohoku-Oki earthquake. The physical processes identified here, driven by rapid coseismic frictional restrengthening and dynamic stress heterogeneity, are likely fundamental controls on rupture behavior in other megathrust settings, carrying significant implications for earthquake dynamics, tsunami generation, and hazard assessment globally.

Results

3D dynamic rupture simulations can capture the nonlinear interactions between seismic wave propagation, fault friction, stress heterogeneity, and fault geometry, leveraging high-performance computing, reaching megathrust earthquake spatial and temporal scales at high resolution [32]. Dynamic rupture simulations have been applied to subduction zones worldwide (e.g., [33]), including the Tohoku-Oki earthquake (e.g., [15, 34]). However, many studies have been restricted to 2D cases with imposed ad-hoc fault friction or stress heterogeneities [13, 14] or simplified friction laws [35], restricting the direct integration of observational constraints and verification.

Our 3D dynamic rupture models (Fig. 1), resolving up to 2 Hz of the seismic wavefield (Methods Sec. “Model geometry and mesh”), investigate physical controls on complex, spontaneous rupture processes by incorporating regional-tectonic constraints ([31], Fig. 1c), and initial stress heterogeneity (Fig. 1d). We construct an initial stress state (Methods Sec. “Prestress and fault strength”) that combines the regional maximum principal stress orientation with stress heterogeneity from a median slip model that captures common slip features among 32 finite-fault slip models ([12], Supplementary Fig. S2). The dynamic models use a realistic slab geometry and high resolution topobathymetry (Fig. 1a), along with fast velocity-weakening rate-and-state friction [21] (Fig. 1b, Extended table E1) and off-fault plasticity (Supplementary Fig. S1). We use depth-varying frictional ($a - b$) parameters to model shallow velocity-strengthening [36] and the downdip limit of the seismogenic zone [2] (Methods Sec. “Fault friction”). We do not impose frictional asperities. Details of the numerical method, and computational requirements are provided in Supplementary Sec. “SM1: Model resolution”.

We identify a preferred 3D dynamic rupture model that minimizes the misfit with seismic moment-rate function and geodetic data constraints. Our preferred model consistently reproduces key observed complexities of the Tohoku-Oki earthquake, including rupture reactivation, depth-varying seismic radiation, large near-trench slip, and rupture arrest. Using a systematic grid-search approach (Methods Sec. “Grid search for initial stress and fault strength”), we constrain the initial stress and fault strength conditions by validating simulation results with geodetic and seismic observations. We quantitatively evaluate the variance reduction of each dynamic rupture scenario and simultaneously minimize misfits with the seismic moment release rate and onshore and offshore static displacements.

The preferred model is selected from an ensemble of 33 simulations which explore variations in (i) initial stress heterogeneity amplitudes (α) and (ii) regionally constrained ratio of fault strength over maximum possible stress drop (R_0), which together govern the earthquake energy balance between the available energy release rate, which sustains rupture propagation, and the fracture energy required for continued rupture growth [37]. The preferred forward simulation achieves variance reductions of 77% and 55% for onshore and offshore geodetic observations,

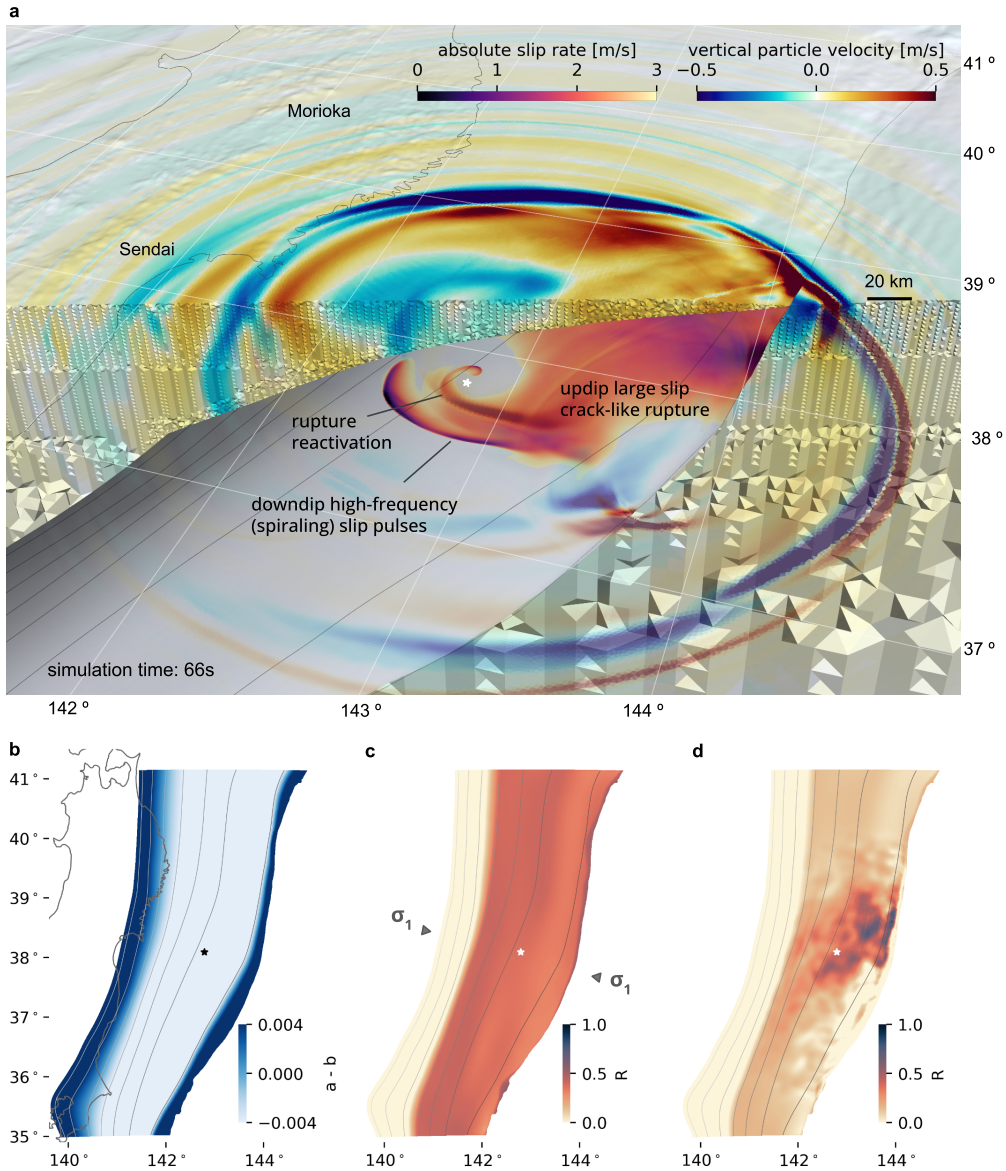


Figure 1: Overview of 3D dynamic rupture simulations of the 2011 Tohoku-Oki earthquake and their initial conditions. Depth contours (gray, 10 km intervals) and hypocenter location (star) are shown in all panels. (a) Snapshot of the simulated absolute slip rate and seismic wavefield evolution (vertical particle velocity) at 66 s, highlighting multiple reactivated slip pulses propagating downdip and crack-like rupture accumulating large slip near the trench. The model incorporates realistic slab geometry and high-resolution topobathymetry within an unstructured tetrahedral mesh refined near the slab and onshore region. (b) Depth-dependent frictional properties ($a - b$, see Methods Sec. “Fault friction”) with velocity-strengthening behavior in the shallow (<9 km) and deep (>45 km) regions, transitioning to velocity-weakening in the seismogenic zone. (c) Laterally homogeneous, depth-dependent ambient stress and frictional strength initial conditions informed by regional tectonics (see Methods Sec. “Prestress and fault strength”), showing the relative prestress ratio R (maximum possible stress drop over frictional strength drop). The principal stress direction (σ_1 at an azimuth of 100° and a plunge angle of 8° , [31]) is marked with arrows. (d) Heterogeneous stress initial conditions combining the ambient background stress shown in (c) and heterogeneous initial stress inferred from the median slip distribution

respectively (Fig. 2a). It features a smooth slip distribution, with major slip concentrated updip of the hypocenter, and a triangular moment-rate function consistent with observations (Fig. 2b). We capture the gradual seismic moment release during the earthquake's initiation phase, in contrast to previous dynamic models (e.g., [14, 34]). Despite the simple slip distribution and moment rate release and the absence of imposed frictional heterogeneity, the model produces substantial rupture complexity, including variations in peak slip rate, rupture speed, and stress drop (Fig. 2c-f), as reported in kinematic slip models (e.g., [5, 38]). The model exhibits an asymmetric rupture pattern (Fig. 2e), with initial southeastward propagation followed by updip and bilateral rupture, consistent with some kinematic slip models [5, 38]. The model yields an average stress drop of 2.4 MPa, matching the average reported stress drop estimates [39]. The coseismic stress drop distribution from our model aligns with the major afterslip pattern of the Tohoku-Oki earthquake between 40-60 km depth [2], where negative stress drop is prominent at the downdip edge of the simulated rupture area.

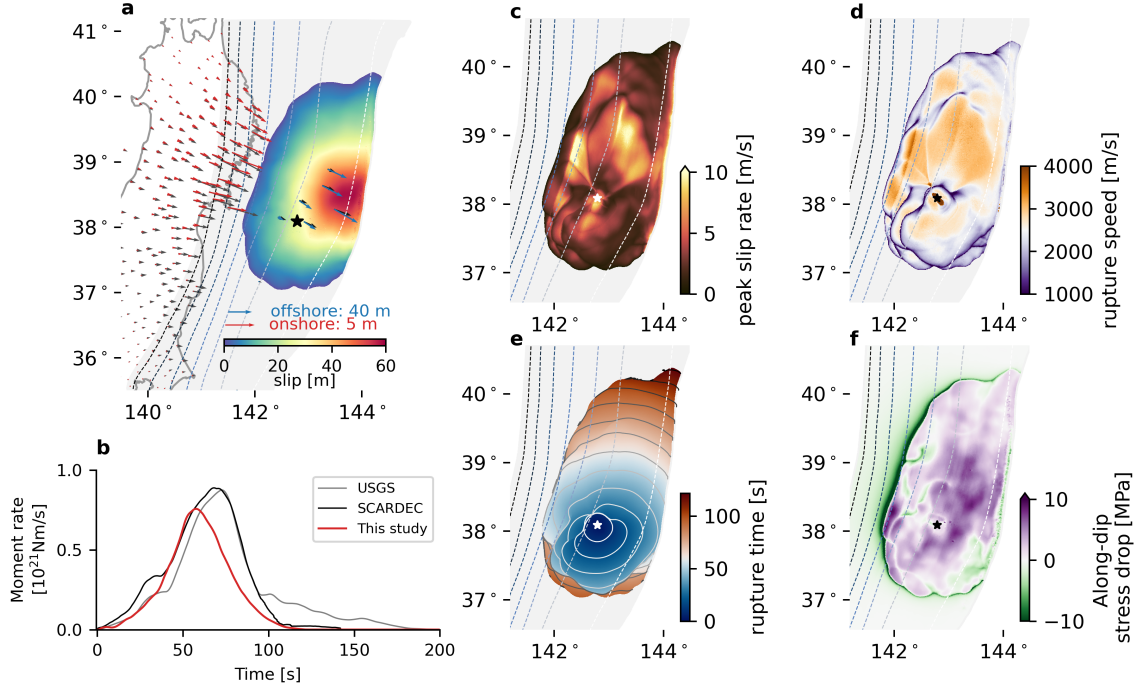


Figure 2: Preferred 3D dynamic rupture scenario of the Tohoku-Oki earthquake constrained by geodetic observations and seismic moment release rate. Gray contours indicate depth (10 km intervals), and the star is the hypocenter location [40]. Rupture extends 200 km along-dip and 360 km along-strike, producing a moment magnitude of $M_W 8.97$ and a duration of 120 s. The total radiated seismic energy is $\approx 7.7 \times 10^{17} J$, within observational estimates of $4.2 - 9.1 \times 10^{17} J$ for the Tohoku-Oki earthquake [4, 7]. (a) Fault slip distribution with comparison between observed and simulated geodetic displacements onshore and offshore. Black arrows denote observed horizontal displacements from offshore and onshore stations. Blue and red arrows represent simulated horizontal displacements offshore and onshore, respectively, achieving variance reductions of 77% (onshore) and 55% (offshore). (b) Synthetic moment rate release compared with observational inferences from teleseismic by the USGS model [40] and SCARDEC inversion results [41]. Heterogeneous spatial distributions of (c) peak slip rate, (d) rupture speed, (e) rupture front timing (10 s intervals, gray contours), and (f) along-dip stress drop.

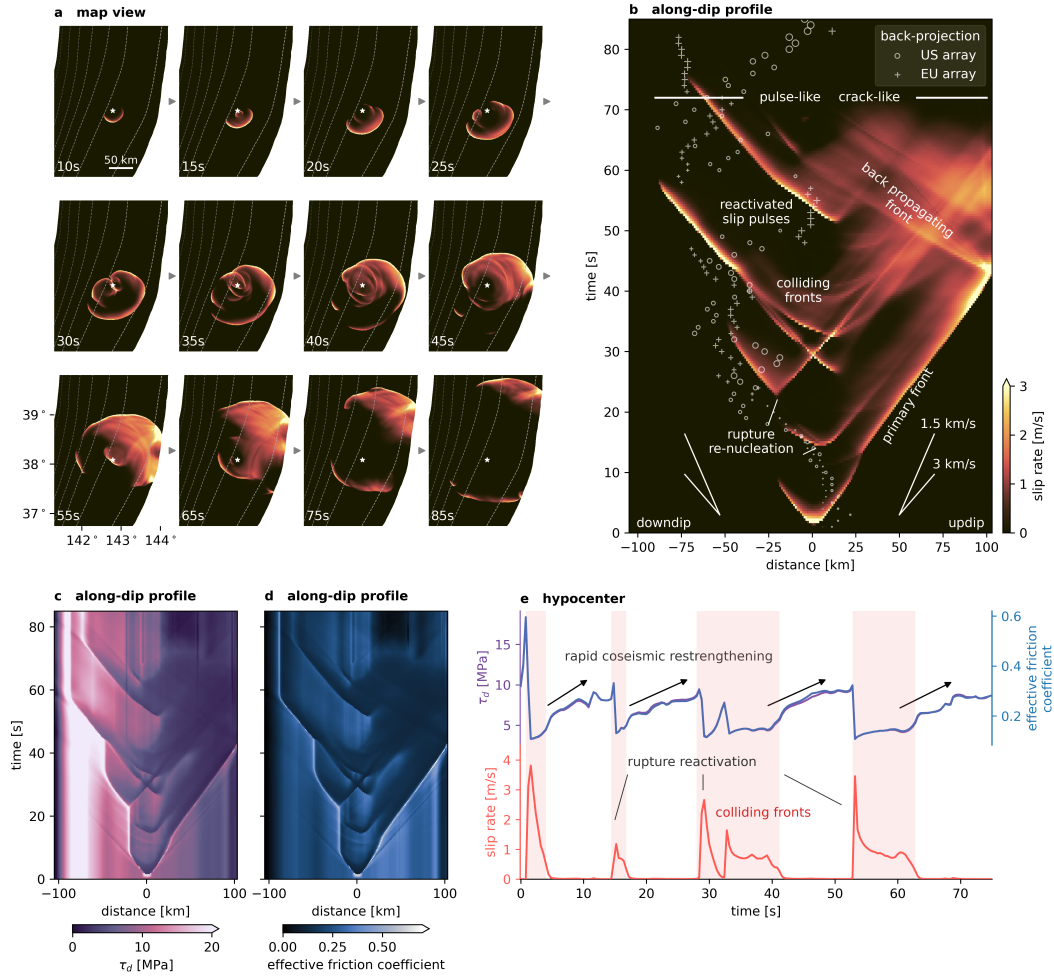


Figure 3: Repeated dynamic rupture reactivation enabled by rapid coseismic weakening and restrengthening during the preferred Tohoku-Oki earthquake dynamic rupture model. (a) Map-view snapshots of rupture evolution from 10 s to 85 s simulation time, showing three main re-nucleation episodes at 15 s, between 25–40 s, and at 50 s. The white star indicates the hypocenter. Similarly “spiraling” rupture fronts have been observed in recent laboratory experiments [42]. Extended Fig. E2 and Supplementary Video S1 show the complete rupture evolution. Extended Fig. E3 shows the detailed evolution of “spiraling” rupture fronts. (b) Slip rate evolution along a dip profile through the hypocenter, highlighting multiple episodes of rupture reactivation. Crosses and circles indicate the locations of high-frequency radiation from back-projection using the US and European arrays, respectively [6]. Rupture propagates faster updip (≈ 2.5 km/s) compared to downdip (≈ 1.7 km/s), matching the observational results from the back-projection analyses [6]. (c)-(d) Temporal evolution of along-dip shear stress (purple) and effective friction coefficient (blue, Methods “Fault friction”) along the hypocentral dip profile, highlighting rapid variations coincident with dynamic rupture reactivation; lighter colors indicate higher values. (e) Time series at the hypocenter of slip rate (red), along-dip shear stress (purple), and effective friction coefficient (blue), showing repeated rupture reactivation (slip rate ≥ 0.05 m/s, shaded red) and rapid frictional restrengthening. Extended Fig. E4 shows updip and downdip time series

Dynamic rupture reactivation driven by rapid coseismic frictional healing

Our dynamic rupture model spontaneously produces episodic pulse- and crack-like slip reactivation originating near the hypocenter (Extended Fig. E2 and Supplementary Video S1). Its complex rupture dynamics include multiple spiraling [42], back-propagating [25, 43], and colliding rupture fronts driven by rapid coseismic frictional weakening and restrengthening. Figure 3a shows the complexity of slip rate evolution through multiple rupture reactivation episodes. The rupture initiates as a primary slip pulse, followed by a secondary slip pulse nucleating at its healing front. Interaction between updip and downdip propagating rupture and healing fronts leads to a successive second, third, and (unsustained) fourth episodes of slip reactivation in the hypocentral region. When the updip propagating rupture fronts reach the seafloor, strong dynamic interactions with the free surface generate trench-reflected, back-propagating phases, which coalesce with secondary arriving rupture fronts to form sustained updip crack-like rupture. In the later stage, rupture simplifies into a bilateral slip pulse propagating along-strike, saturating the seismogenic zone width before spontaneously arresting.

Our model explains the observed contrast between the slow downdip rupture propagation speed [6] and the faster updip speed [3, 5, 38]. Figure 3b shows how episodic pulse-like rupture reactivation successively extends the rupture duration downdip, producing a slower apparent rupture speed (≈ 1.5 km/s). In contrast, the updip rupture front propagates steadily as a primary crack-like rupture front at ≈ 2.5 km/s.

Rapid coseismic restrengthening emerges as the principal mechanism controlling repeated reactivation, causing a fault portion to slip and stop more than once during the same earthquake. The mechanisms driving rupture reactivation are illustrated by the along-dip evolution of shear stress and frictional strength (Figs. 3c–d), and by the corresponding time series at the hypocenter (Fig. 3e).

Initially, as slip rate increases, both along-dip shear stress and effective friction coefficient sharply rise due to the instantaneous response of rate-and-state friction to slip rate changes (the direct effect, [19]), quickly followed by rapid weakening [21, 22], causing dynamic stress drops of up to 10 MPa (Fig. 3e). As slip rate subsequently ceases, a healing front follows. The growing slip pulse gradually concentrates shear stress in its hypocentral region eventually overcoming local fault strength and reactivating slip, consistent with theoretical predictions for singular, self-similar pulse-like rupture [44] and simpler 2D numerical simulations [25]. This process repeats multiple times, resulting in six distinct slip episodes at the hypocenter in our preferred rupture model. Notably, all secondary ruptures are pulse-like in the downdip direction and evolve into crack-like ruptures in the updip region, mirroring the depth-dependent behavior of the initial primary rupture.

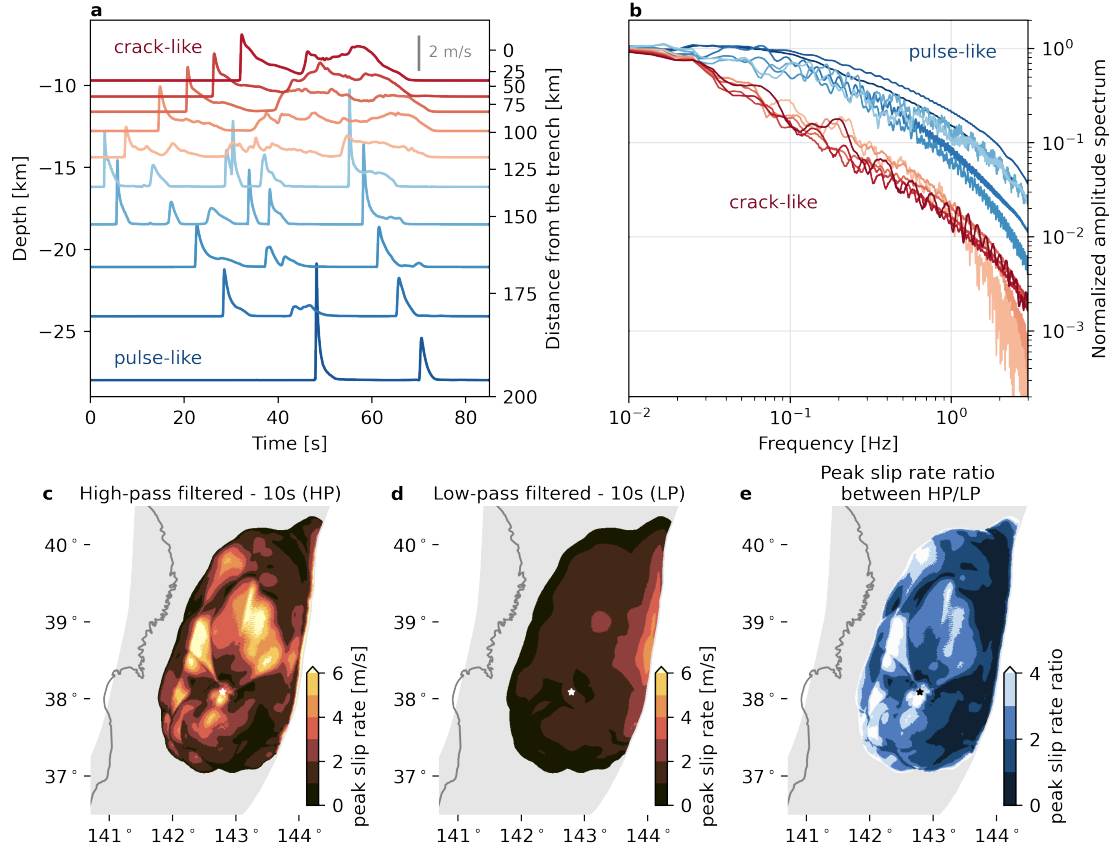


Figure 4: Depth-varying rupture styles featuring downdip short-duration slip pulses and updip large-slip crack-like ruptures. (a) Slip-rate evolution with depth, highlighting crack-like ruptures shallower than 15 km depth (red) and pulse-like ruptures at greater depths (blue). (b) Normalized amplitude spectra of the slip rates, illustrating systematically higher-frequency content in downdip pulses compared to the shallower crack-like ruptures. The shallow crack-like rupture spectra follow a -1 slope over the 0.02-1 Hz range, whereas the pulse-like rupture exhibits a shallower -0.7 slope within the same frequency band. (c–d) Spatial distribution of high-pass filtered (HP) and low-pass filtered (LP) peak slip rates, respectively. (e) Spatial variation in the ratio of high-frequency to low-frequency peak slip rates (HP/LP). Shallow regions (<15 km depth) exhibit predominantly crack-like rupture with low HP/LP ratios, while downdip and hypocentral areas show pulse-like ruptures enriched in high-frequency content, consistent with observations from back-projection and regional strong-ground motion analyses [6, 45].

Downdip slip pulses and updip crack-like rupture

Observational studies, including teleseismic back-projection [6], regional strong-ground motion analyses [45], and finite-fault inversions [5, 38], have consistently documented depth-dependent seismic radiation characteristics in the Tohoku-Oki earthquake. In our preferred model, we observe depth-varying dynamic rupture styles, characterized by short-duration slip pulses [46] radiating high-frequency seismic waves downdip and prolonged crack-like rupture accumulating large slip updip (Fig. 4). Figure 4a highlights contrasting slip-rate functions across different depths. At depths shallower than 15 km, rupture propagation is crack-like, characterized by continuous slip and prolonged rise times exceeding 50 s. In contrast, rupture transitions to sharp slip pulses as it propagates deeper than 15 km, each with rise times less than 10 s. These depth-dependent rupture styles become particularly evident during 30–80 s rupture time, when multiple reactivated rupture fronts are present, and the deeper ruptures manifest discrete short-duration pulses (Fig. 4a, Extended Fig. E4). This rupture-style variability directly influences the associated seismic radiation. Figure 4b shows normalized slip-rate amplitude spectra, revealing that shallow crack-like rupture episodes are depleted in high-frequency energy than the deeper pulse-like rupture portions.

Observational studies indicate that high-frequency radiation inversely correlates with the total slip (e.g., [5, 7]). Our preferred dynamic rupture model reproduces these observations, showing the amplitude ratio of high-pass to low-pass filtered peak slip-rate function at 10 s period reaching approximately 400% in the downdip and hypocentral regions (Fig. 4e). Furthermore, the multiple reactivated downdip slip pulses can explain migrating downdip and hypocentral high-frequency seismic radiation imaged through back-projection methods (Fig. 3b; [6]). In contrast, shallow regions are dominated by large slip occurring primarily at low frequencies, consistent with crack-like behavior suggested in finite-fault models (e.g., [5, 38], Fig. 4c–e).

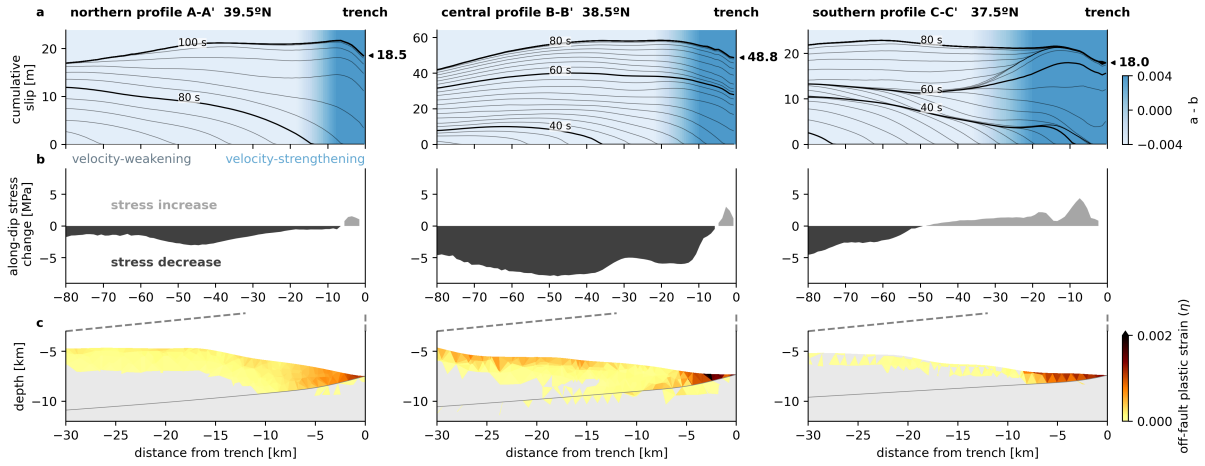


Figure 5: Large near-trench slip occurs despite shallow velocity-strengthening frictional behavior, shallow off-fault plastic deformation, and negative stress drop. Along-dip profiles of slip, stress drop, and off-fault deformation at northern (39.5° , first column), central (38.5° , second column), and southern (37.5° , third column) cross-sections. (a) Evolution of cumulative slip at 2 s (thin lines) and 20 s intervals (thick lines). Background color shading indicates frictional behavior, transitioning from velocity-weakening (light blue) at depth to velocity-strengthening (dark blue) near the trench. Bold values at the right indicate the fault slip amplitude at the trench. (b) Along-dip shear stress change ($\Delta\tau$), with dark gray representing stress decrease and light gray representing stress increase. (c) Close-up view of the distribution of off-fault plastic strain (color shading, quantified as η , Methods Sec. “Off-fault plasticity”) and the megathrust interface geometry (gray line).

Large slip to the trench despite shallow velocity-strengthening, off-fault plasticity, and negative stress drop

Shallow slip reaching the trench is critical for assessing tsunami hazards associated with large megathrust earthquakes. Our simulation demonstrates substantial near-trench slip, driven by rapid coseismic frictional weakening, despite competing effects from shallow off-fault plastic deformation, velocity-strengthening frictional behavior, and the associated negative stress drop. Figure 5a presents three along-dip profiles of slip from south to north. The modeled trench slip magnitudes of 18.5 m, 48.8 m, and 18.0 m at the southern, central, and northern cross-sections are comparable to differential bathymetry measurements, which indicate horizontal displacements of approximately 50 m-70 m at the central region and up to 20 m to the northern and southern extents (Extended Fig. E5, [9, 47]).

In our model, dynamic frictional weakening effectively sustains shallow rupture propagation, enabling up to 50 m of slip near the trench. The velocity-strengthening friction (≥ 9 km depth) adopted in our model is based on laboratory friction measurements of borehole samples in the shallow high-slip region of the Tohoku-Oki earthquake and the expected behavior of clay-rich rock samples [36]. Additionally, off-fault plastic deformation dissipates seismic energy in the uppermost 10 km (Fig 5, [15]), though its overall contribution remains limited, accounting for only 2.9% of the total on-fault seismic moment. Lastly, our assumed initial stress state (Extended Fig. E1b) features low to negative shear stress near the trench, implying limited near-trench strain accumulation prior to the Tohoku-Oki earthquake [48]. Nonetheless, the collective effects of velocity-strengthening friction, off-fault plasticity, and low prestress conditions only modestly reduce trench slip, by about 10% relative to the maximum slip further down-dip (Fig. 5). This reduction in trench slip aligns with near-trench bathymetric evidence of inelastic deformation and a decrease in horizontal displacement at the trench [49].

Spontaneous along-strike rupture arrest

Our preferred model successfully reproduces the spontaneous along-strike rupture arrest of the Tohoku-Oki earthquake by incorporating data-informed stress heterogeneity rather than prescribing ad hoc frictional or structural barriers. In linear elastic fracture mechanics, dynamic rupture arrest occurs where available strain energy becomes insufficient to exceed local fracture energy, halting further rupture propagation [17, 50]. In our simulation, rupture arrest results from strain energy depletion, as evidenced by a reduction in breakdown energy near the fault areas where rupture terminates (Extended Fig. E6, Methods Sec. “Breakdown work density”). During the later stages of rupture (70–120 s), bilateral rupture pulses propagate into regions with lower relative prestress levels (R) (Fig. 1 d), progressively decreasing in slip rate amplitude, rupture speed, and pulse width (Fig. 2d,e).

An exception occurs in the shallow northern slab section, where rupture arrest is delayed. Here, a localized region of elevated relative prestress, situated northeast and updip of the hypocenter (Fig 1d), generates a high slip rate rupture pulse propagating toward the northern shallow margin (Fig. 3a). This interaction facilitates extended shallow rupture in the northern slab region, producing uplift patterns consistent with those derived from tsunami waveform inversions (Extended Fig. E5, e.g., [51]).

In contrast, alternative simulations that use solely depth-dependent prestress conditions informed by regional principal stress orientations without stress heterogeneities fail to spontaneously arrest rupture (Fig 1b, [31]). Under comparable average prestress levels, these laterally homogeneous prestress models result in rupture of the entire megathrust, yielding an unrealistic moment magnitude of $M_W 9.61$ and a too prolonged rupture duration of 220 s (Extended Figure E7).

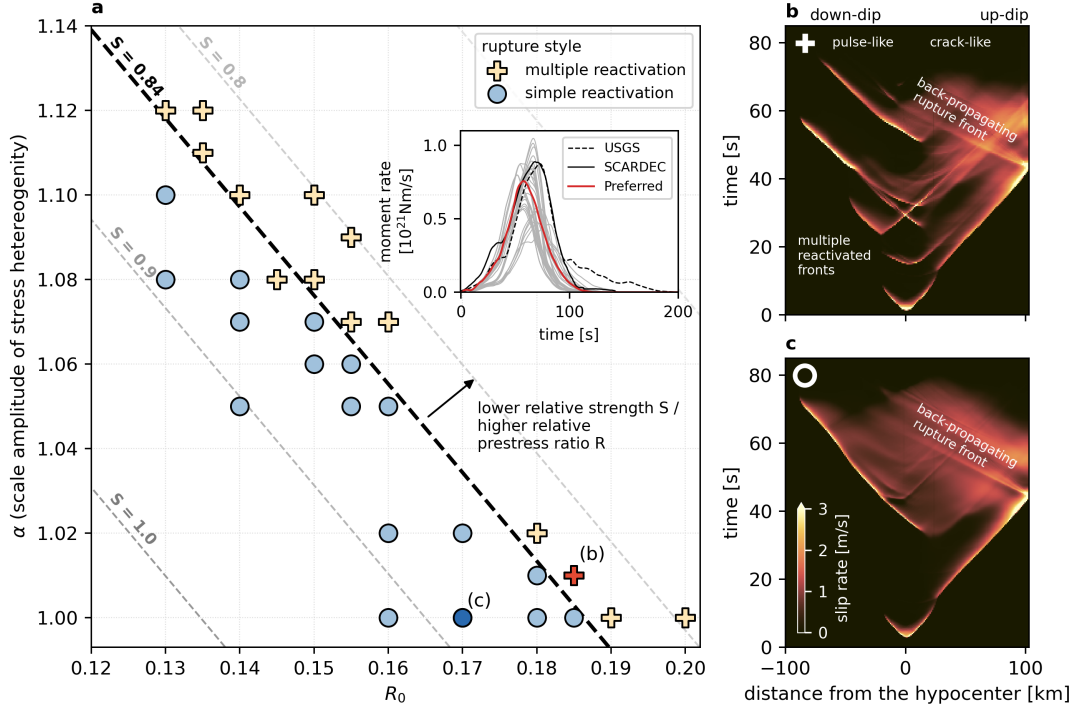


Figure 6: (a) Phase diagram showing how variations in stress heterogeneity amplitude (α) and regional ambient stress level (R_0) control rupture style. Blue circles represent a family of dynamic rupture models dominated by prominent pulse-like rupture with free-surface reflection and back-propagating crack-like rupture, while yellow crosses denote models exhibiting repeated rupture reactivation near the hypocenter resembling the preferred model. The preferred model (red cross) and an exemplary simpler model (light blue circle) are indicated, with their corresponding along-dip slip-rate evolutions shown in (b) and (c), respectively. Dashed contours illustrate the variation of hypocentral seismic S ratio (initial strength excess over dynamic stress drop), with the thick dashed line marking the transition boundary between rupture styles. We observe that the amplitude of stress heterogeneity (α) primarily controls peak slip magnitude, whereas the regional ambient stress level (R_0) largely determines rupture extent in both families of dynamic rupture models. The inset compares the moment-rate functions of all models (gray lines), highlighting the preferred model (red), the USGS inversion [40] (black dashed), and the SCARDEC inversion result [41] (solid black). (b–c) Along-dip slip-rate evolution illustrating the rupture reactivation family (preferred model) and the simpler rupture family, respectively.

Discussion

We explore how rupture evolution depends on the relative prestress level and the amplitude of stress heterogeneity by systematically varying α and R_0 , which represent the stress heterogeneity amplitude and regional ambient stress level. We find two distinct dynamic rupture styles (Fig. 6): one resembling the preferred model, and another dominated by a prominent updip-propagating pulse that reflects off the free surface, back-propagates, and transitions to crack-like rupture.

We find that our preferred rupture style requires low fault strength compared to the dynamic stress drop, corresponding to a low seismic S ratio [52]. Lower effective normal stress and fault strength or higher initial shear stress favor reactivation-dominated scenarios. The abrupt transition in rupture behavior with changes in prestress is consistent with prior work (e.g., [25, 53]). However, in simple theoretical and numerical models, higher prestress downdip is generally expected to favor crack-like rupture, while lower prestress should promote updip pulse-like propagation. Models without stress heterogeneity (Method Sec. “Regional stress rupture model without stress heterogeneity”), exhibit a pulse-to-crack rupture transition, characterized by a distinguishable rupture reactivation episode (Extended Figs. E8, E9, Supplementary Fig. S6, and Video S2).

In contrast, heterogeneous stress conditions in our models cause locally low prestress regions, particularly near the hypocenter and downdip, which facilitate the formation of healing fronts [53], which induce pulse-like ruptures. These healing fronts lead to stress recovery along previously ruptured segments [44], facilitating subsequent reactivation. All reactivated ruptures are pulse-like down-dip, due to the locally heterogeneous nature of the slip left behind by the primary rupture front which correlates with the distribution of the primary residual stresses [25]. Updip, reactivated fronts coalesce with the surface-reflected primary rupture to form a sustained crack-like rupture (Fig. 4a, Extended Fig. E4).

Our simulations indicate that large megathrust earthquakes may exhibit mixed pulse- and crack-like rupture modes. The long-standing debate over whether earthquake rupture propagates predominantly as pulses or cracks has important implications for frictional behavior and earthquake energy partitioning [18, 46]. While models based on linear elastic fracture mechanics commonly assume uniform breakdown energy [17, 54], mixed rupture styles, repeated rupture reactivation, and rapid frictional restrengthening collectively lead to heterogeneous breakdown energy without the presence of frictional heterogeneity (Extended Fig. E6).

While beyond the scope of this work, our simulations can be extended to explore additional effects that are potentially important but challenging to observe, including sediment heterogeneity [55], accretionary wedge geometry [56], interface roughness, and upper plate structure [57].

Using 3D dynamic rupture simulations, we demonstrate that the complex rupture behavior of the Tohoku-Oki earthquake can spontaneously arise from dynamic rupture processes. We highlight that stress heterogeneity, although challenging to quantify, can be informed by existing observational data and fundamentally controls the complexity and scale of dynamic rupture. Our models capture episodic re-nucleation in the hypocentral region, the co-existence of short-duration, spiraling slip pulses at depth and shallow crack-like rupture with large slip near the trench, and spontaneous rupture arrest. Similar rupture complexities have been documented in other large megathrust earthquakes, including the 2010 M_W 8.8 Chile earthquake [58], and the 2019 M_W 8.0 Northern Peru earthquake [59], and thus may be expected and should be prepared for in future megathrust earthquakes. To this end, this work provides a robust, self-consistent framework applicable to other megathrust settings towards physics-based earthquake and tsunami hazard assessment worldwide.

Acknowledgments

We thank Thomas Ulrich and the SeisSol team for their help in using SeisSol, and Elisa Tinti, Yoshihiro Kaneko, and Dmitry Garagash for insightful discussions.

Data availability

We use the open-source software package SeisSol version 1.2.0 (www.seissol.org), available at <https://github.com/SeisSol/SeisSol>, commit *8cddb43c* on the master branch to perform all dynamic rupture simulations presented in this study. Instructions for downloading, installing, and running the code are available in the SeisSol documentation at <https://seissol.readthedocs.io/>. All data and model parameter files required to reproduce the dynamic rupture scenarios can be downloaded from <https://zenodo.org/records/15117294>. The onshore Geodetic data are provided by the Geospatial Information Authority (GSI) [60].

Funding

This work was supported by NSF grants EAR-2143413 and EAR-2121568. AAG acknowledges additional support from NASA (grant No. 80NSSC20K0495), NSF (grants EAR-2225286, OAC-2139536, OAC-2311208), the European Union’s Horizon 2020 Research and Innovation Programme (grant No. 852992), Horizon Europe (grant No. 101093038, 101058129, and 101058518) and the Statewide California Earthquake Center (SCEC award 25341). We gratefully acknowledge the Texas Advanced Computing Center (TACC, NSF grant No. OAC-2139536) and the Gauss Centre for Supercomputing (LRZ, project pn49ha) for providing supercomputing time. Additional computing resources were provided by the Institute of Geophysics of LMU Munich [61].

Author contributions

JWCW: Data Curation, Methodology, Formal analysis, Investigation, Writing - Original Draft, Visualization. AAG: Conceptualization, Software, Methodology, Formal Analysis, Resources, Writing - Original Draft, Supervision, Validation, Funding acquisition. WWF: Conceptualization, Methodology, Resources, Writing - Review & Editing, Supervision, Validation, Funding acquisition.

Competing interests

The authors declare no competing interests and no conflict of interest.

Methods

We perform 3D dynamic rupture simulations of the 2011 M_w 9.0 Tohoku-Oki earthquake that simultaneously solve for seismic wave propagation, on-fault frictional failure, and off-fault inelastic deformation. 2D and 3D dynamic rupture simulations have been applied to subduction zones worldwide [e.g., 33, 35, 62–66], including the Tohoku-Oki earthquake [13–15, 34, 67, 68]. Here, for the first time, we present fully dynamic 3D rupture simulations of the Tohoku-Oki earthquake incorporating rapid velocity-weakening and coseismic frictional restrengthening, constrained by observationally informed stress heterogeneity. Unlike previous dynamic rupture models that prescribed frictional or stress asperities, our simulations spontaneously reproduce the observed complex rupture behavior—including repeated rupture reactivation, depth-dependent rupture styles, and realistic trench slip—solely through dynamic friction evolution and stress conditions.

We use the open-source software SeisSol (<https://seissol.org>) for all dynamic rupture simulations on two supercomputers, SuperMUC-NG, at the Leibniz Supercomputing Center, Germany, and Frontera, at the Texas Advanced Computing Center, United States. SeisSol employs the Arbitrary High-order Derivative (ADER) Discontinuous Galerkin (DG) method [69], which enables higher-order accuracy in space and time on unstructured tetrahedral meshes, which are well-suited to capture geometric complexities, including shallowly dipping megathrust interfaces in subduction zones [e.g., 35, 63]. SeisSol is optimized for high-performance computing [e.g., 32, 70, 71] and verified in dynamic rupture community benchmarks [72–75]. We employ SeisSol with sixth-order accuracy in time and space, i.e., the polynomial order of the basis functions is $p = 5$.

Model geometry and mesh

Our 3D dynamic rupture models incorporate realistic megathrust geometry, high-resolution topobathymetry, and velocity-aware adaptive mesh refinement to accurately capture rupture processes and seismic wave propagation up to 2 Hz [76]. Our megathrust geometry is adapted from the 3D Japan Integrated Velocity Structure Model geometry (JIVSM) [77, 78], which is based on seismic imaging, waveform inversion, and seismicity studies. We extract the top layer of the oceanic plate as the megathrust interface. To ensure the interface connects to the trench, we extend and smooth the interface to the USGS trench with a 12° extension from the surface following Wong *et al.* [12]. The constructed megathrust interface spans a region from 35°N to 41°N and from 139.5°E to 145°E , extending approximately 700 km along strike, 250 km along dip, and reaching a depth of 80 km (Fig. 1). This large extent of the megathrust geometry can prevent model boundary effects on dynamic rupture arrest.

Our model incorporates realistic topobathymetry using the Geobco dataset at 15 arc s (380 m)

resolution [79]. We use a 1D velocity structure consisting of five layers, which we modify from [80] (Supplementary table S1) by prescribing a 20% shear modulus reduction in the two uppermost layers. This adjustment accounts for the presence of lower-rigidity materials in shallow subduction zone regions and closely matches the average shear modulus derived from the 3D JIVSM velocity model at equivalent depths.

Our structure model is refined near the fault interface to accurately resolve the process zone at the rupture tip, near the free surface to capture topobathymetry, and near Honshu Island to resolve the seismic wavefield up to 2 Hz (Supplementary Sec.: “SM1: Model resolution”, Fig. S8). The process zone width Λ [81] is defined as the area behind the rupture front in which the shear stress decreases from the static value to the dynamic value. The resulting unstructured tetrahedral mesh consists of 50.3 million elements, and one simulation requires 58,000 CPU hours on Frontera and 64,000 CPU hours on SuperMUC-NG. The mesh uses the following Cartesian projection: WGS84/UTM transverse mercator centered at (143°E, 39°N).

Fault friction

We use a fast velocity-weakening rate-and-state friction law that replicates the severe coseismic friction reduction observed in high slip-rate laboratory experiments [22, 82], including studies of using drilled samples from the Japan subduction zone [23, 83]. Such pronounced weakening at elevated slip rates can result from flash heating of highly stressed, short-lived contact asperities and thermal pressurization due to shear heating of pore fluids [e.g., 84–87].

This friction law allows the megathrust fault interface to operate under low average shear stress while producing realistic fault slip and stress drop during dynamic rupture [21, 26], and promoting complex rupture styles including cascading ruptures across multi-fault systems [e.g., 25, 88–93]. Low average shear stress conditions align with the limited thermal signature of the Tohoku-Oki earthquake, which may imply rupture under low ambient stress levels [94]. Although this friction law has been extensively used in 2D simulations to examine its control on rupture dynamics [e.g., 21, 95, 96] and in 3D models of crustal earthquakes [e.g., 26, 97], it has not yet been explored in a 3D full-scale model of a large megathrust earthquake.

We use the formulation suggested in the community benchmark problem TPV104 of the Southern California Earthquake Center [74], which is similar to the friction law introduced by Dunham *et al.* [95]. All frictional parameters are listed in Extended Table E1.

In the rate-and-state friction framework, frictional strength depends on both the state of the slipping surface and the current slip rate [20, 98]. The shear traction τ , is assumed to equal fault strength, and is given by

$$\tau = f(V, \theta) \sigma'_n. \quad (1)$$

f is the effective friction coefficient, V is the slip rate, θ is the state variable and σ'_n is the

effective normal stress.

The frictional coefficient f depends on V and θ , as

$$f(V, \theta) = a \sinh^{-1} \left[\frac{V}{2V_0} \exp \left(\frac{\theta}{a} \right) \right], \quad (2)$$

where a is the direct-effect parameter and V_0 is the reference velocity. The evolution of θ is governed by

$$\frac{d\theta}{dt} = -\frac{V}{L}(\theta - \theta_{ss}), \quad (3)$$

where L is the characteristic slip distance, t is time, and θ_{ss} is the steady-state value of the state variable, which is given by

$$\theta_{ss}(V) = a \ln \left[\frac{2V_0}{V} \sinh \left(\frac{f_{ss}V}{a} \right) \right]. \quad (4)$$

The steady-state friction coefficient f_{ss} is given by

$$f_{ss}(V) = f_w + \frac{f_{LV_{ss}}(V) - f_w}{(1 + (V/V_w)^4)^{1/4}}, \quad (5)$$

where V_w is the onset of the weakening velocity, f_w is the fully weakened friction coefficient, and the steady-state low-velocity friction coefficient is:

$$f_{LV_{ss}} = f_0 - (b - a) \ln(V/V_0), \quad (6)$$

with b as the state-evolution parameter, and f_0 as the reference friction coefficient. The steady-state friction behavior is asymptotic, such that $f_{ss}(V) \approx f_{LV_{ss}}(V)$ for $V \ll V_w$ and $f_{ss}(V) \approx f_w$ for $V \gg V_w$. This behavior aligns with laboratory observations, capturing classic rate-and-state frictional behavior at low sliding velocities and pronounced frictional weakening at high sliding velocities.

Velocity-strengthening, $(a - b) > 0$, friction describes materials whose frictional strength increases with rising slip rate, thus stabilizing fault slip. Conversely, velocity-weakening, $(a - b) < 0$, friction characterizes materials that decrease in strength with increasing slip rate, facilitating the nucleation and propagation of unstable slip [16, 99].

In our models, we prescribe a depth-dependent distribution of $(a - b)$ to represent realistic frictional behavior along the megathrust interface. The shallow portion (< 10 km depth) of the Japan subduction zone is characterized by velocity-strengthening friction, consistent with laboratory measurements of frictional behavior of clay-rich accretionary wedge material at low slip velocities [23, 36, 100, 101]. This velocity-strengthening region is constrained by the transition depth from accretionary wedge to bedrock, as defined by the JIVSM [77, 78]. Between

10–45 km depth, we define the seismogenic zone by parameterizing velocity-weakening friction. Further downdip, between 40–50 km depth, friction gradually transitions back to velocity-strengthening, consistent with observed downdip limits of seismicity and diverse faulting behaviors [102, 103]. We assign uniform frictional parameters along strike within each depth interval, except near the hypocenter, where a modified state evolution distance is imposed for smooth rupture nucleation (Supplementary Section ‘SM2: Nucleation’’).

Depth-dependent effective normal stress

Pore fluid pressure plays an important role in controlling the effective normal stress and thus the stress conditions governing earthquake rupture dynamics [e.g., 104]. Drilling observations and seismic reflection studies in the Japan subduction zone have documented elevated pore fluid pressure within the accretionary wedge and along the shallow fault interface, reaching 80-95% of lithostatic stress [105, 106]. Stress orientation analyses support elevated ambient pore fluid pressure at seismogenic depths [107]. The lithostatic stress is defined as $P_{litho}(z) = \int_0^z (\rho_i g h_i) dz$, where the subscript i refers to the respective layer in the velocity model and $g = 9.81 m/s^2$ is the gravitational acceleration. We assume that pore fluid pressure reaches 90% of lithostatic stress in all layers. This assumption results in depth-dependent effective normal stress and relatively low fault strength everywhere (Extended Fig. E1c).

Off-fault plasticity

We account for off-fault inelastic energy dissipation using a Drucker-Prager visco-elasto-plastic rheology [108, 109]. Models incorporating off-fault plasticity require specifying initial stress, bulk friction, and cohesion throughout the entire simulation domain. We employ a depth-dependent cohesion model following [35] and motivated by laboratory-inferred shallow low cohesion [36, 100], where bulk cohesion $C(z)$ varies linearly with effective confining pressure:

$$C(z) = C_0 + C_1(z)\sigma'_c, \quad (7)$$

where $C_1(z)$ represents rock hardening with depth and $\sigma'_c = \sigma_{litho} - P_f$ is the effective confining stress. We set C_0 to 1.0 MPa to represent partially consolidated sediments, while C_1 linearly reduces from 1 to 0 at depths shallower than 18 km.

The Drucker-Prager yield criterion is given by

$$\tau_c = C(z) \cos(\Phi) - \sigma_m \sin(\Phi), \quad (8)$$

where $\Phi = \arctan(f')$ is the internal angle of friction and $\sigma_m = \Sigma_{n=1}^3 \sigma_{ii}/3$ as the mean stress.

The closeness-to-failure (CF) metric [110] is defined as the ratio between the magnitude of the deviatoric shear stress (J_2) and τ_c :

$$CF = \frac{\sqrt{J_2}}{\tau_c}. \quad (9)$$

This parameterization results in shallow regions (above 10 km depth) being close to yielding ($CF \approx 0.8$) under both preferred and regional stress conditions (Supplementary Fig. S1).

The total seismic moment $M_{0,t}$ is the sum of the moment due to the slip on fault, $M_{0,e}$, and the moment due to off-fault plastic strain, $M_{0,p}$ [35, 111], as:

$$M_{0,p} = \sum_{i=1}^N \mu V \eta, \quad (10)$$

where μ is the rigidity, V is the volume of each tetrahedral element i , and η is a scalar quantity measuring the accumulated off-fault plastic strain at the end of the dynamic rupture simulation. Following [112], η is defined as:

$$\eta(t) = \int_0^t \sqrt{\frac{1}{2} \dot{\epsilon}_{ij}^p \dot{\epsilon}_{ij}^p} dt, \quad (11)$$

with $\dot{\epsilon}_{ij}^p$ as the 3D inelastic strain rate tensor.

The contribution of plastic strain to the total moment is small for our rupture models. Ratios of $M_{0,p}/M_{0,e}$ for both the heterogeneous and regional relative prestress rupture scenarios are on the order of a few percent (preferred model: 2.9%), consistent with 2D dynamic-rupture simulations and large scale megathrust simulation [35, 111, 113] at comparable relative prestress levels.

Prestress and fault strength

Variations in prestress significantly influence rupture style and complexity [25, 53, 95, 114]. However, the prestress and strength conditions that govern earthquake rupture are challenging to directly constrain by observations [39, 115]. Previous dynamic rupture models of the Tohoku-Oki earthquake have relied on prescribed frictional asperities [e.g., 15, 68, 89] and, in some cases, additional stress asperities [e.g., 13, 14, 67, 116–118], both of which require ad-hoc assumptions.

We define the initial stress tensor s_{ij} as a linear combination of the regional-tectonically constrained stress tensor b_{ij} and the stress changes inferred from finite-fault slip models c_{ij} , following [119, 120]. The initial full stress tensor s_{ij} is defined as:

$$s_{ij}(x, y, z) = \Omega(z)(b_{ij}(x, y, z) + \alpha c_{ij}(x, y, z)) + (1 - \Omega(z))\sigma'_n(x, y, z)\delta_{ij}, \quad (12)$$

with $\Omega(z)$ as a depth-dependent modulation function smoothly tapering deviatoric stresses below the seismogenic zone (45 km), α as a scaling factor controlling the amplitude of stress heterogeneity, and δ_{ij} is the Kronecker Delta.

Dynamic rupture simulations often exhibit strong trade-offs between friction and initial stress conditions [e.g., 121]), which can be characterized by the relative prestress ratio R between the maximum potential stress drop and frictional strength drop [122]. Following Ulrich *et al.* [26], to define R in our velocity-weakening rate-and-state friction framework, we approximate peak shear strength as $f_0\sigma'_n$ and residual strength as the fully weakened frictional state, $f_w\sigma'_n$. During rupture, the shear stress level typically approaches this fully weakened frictional state (Extended Fig. E4). R is then defined as

$$R = \frac{\tau_0 - \mu_d\sigma'_n}{(\mu_s - \mu_d)\sigma'_n} \approx \frac{\tau_0 - f_w\sigma'_n}{(f_0 - f_w)\sigma'_n}, \quad (13)$$

where τ_0 is the initial shear traction projected from s_{ij} on the 3D megathrust interface.

Alternatively, initial stress and fault strength can be characterized by the seismic ratio S [52], which represents the ratio of initial strength excess to maximum dynamic stress drop:

$$S = \frac{\mu_s\sigma'_n - \tau_0}{\tau_0 - \mu_d\sigma'_n} \approx \frac{f_0\sigma'_n - \tau_0}{\tau_0 - f_w\sigma'_n}, \quad (14)$$

with a direct relationship between R and S :

$$R = \frac{1}{1 + S}. \quad (15)$$

The R and S ratios capture different aspects of the balance between available strain energy and fracture energy, thus influencing dynamic stress drop and acceleration or deceleration of the rupture front. For non-planar fault geometries and spatially variable prestress and initial fault strength, these ratios vary across the fault interface(s). As detailed below (Sec. Ambient prestress), prescribing a regionally uniform $R_0 \geq R$, defined as the R -value for an optimally oriented fault segment, allows us to constrain the amplitude of deviatoric stresses relative to the frictional strength drop, while naturally incorporating stress variability due to the megathrust geometry.

Ambient prestress

The ambient prestress tensor b_{ij} is constrained using observed regional stress orientations, and assumed fault-fluid pressure and Mohr–Coulomb frictional failure criteria, following [35]. We prescribe a uniform regional stress field orientation based on the inferred principal stress orientations along the Japan subduction zone from the World Stress Map [31], with the maximum

principal stress oriented at an azimuth of 100° and a plunge angle of 8° . The magnitudes of the principal stresses s_i are determined through the stress shape ratio ν as:

$$\nu = \frac{s_2 - s_3}{s_1 - s_2}. \quad (16)$$

We use $\nu = 0.5$ in all simulations, again based on the World Stress Map [31].

Following the notation of Aochi [122], the Mohr-Coulomb failure criteria is defined as:

$$P = (s_1 + s_3)/2 \quad \text{and} \quad ds = (s_1 - s_3)/2. \quad (17)$$

with $(P, 0)$ being the center of the Mohr-Coulomb circle and ds as its radius. Principal stresses s_i are related to P , ds and ν as

$$\begin{aligned} s_1 &= P + ds, \\ s_2 &= P - ds + 2\nu ds, \\ s_3 &= P - ds. \end{aligned} \quad (18)$$

The effective mean confining stress $\sigma'_c = (s_1 + s_2 + s_3)/3$ is given by:

$$\sigma'_c = P + (2\nu - 1)ds/3. \quad (19)$$

The shear and normal stresses (τ and σ_n) acting on a fault plane oriented at an angle Φ relative to the maximum principal stress are:

$$\begin{aligned} \tau &= ds \sin 2\Phi, \\ \sigma_n &= P - ds \cos 2\Phi, \end{aligned} \quad (20)$$

In this framework, an optimally oriented fault plane is defined as the orientation that, under uniform initial stress and loading rate, reaches frictional failure first, maximizing the shear-to-normal stress ratio to equal the static friction coefficient μ_s . Its optimal orientation relative to the maximum principal stress direction is thus:

$$\Phi = \pi/4 - 0.5 \arctan(f_0 \sigma'_n). \quad (21)$$

The deviatoric stress magnitude ds is derived by combining Eqs. 13, 19, and 20:

$$ds = \frac{\sigma'_c}{\sin 2\Phi / (f_w + (f_0 - f_w)R_0) + (2\nu - 1)/3 + \cos 2\Phi}. \quad (22)$$

Based on a given regional optimal relative prestress ratio R_0 , we can compute the principal stress amplitude s_i using Eqs. 18, 19, and 22. The orientations of the principal stress axes are constrained by the azimuth $SH_{max} = 100^\circ$ and the plunge angle $\theta = 8^\circ$.

Data-informed shear stress heterogeneity

We incorporate initial shear stress heterogeneity informed by finite-fault slip models. We adopt the median slip distribution derived from 32 published finite-fault models of the Tohoku-Oki earthquake [12]. This median slip model has a simple slip distribution with a smooth, circular patch up-dip of the hypocenter, showing significant slip extending to the trench. The model robustly captures large-scale slip features common across these models and can successfully reproduce key geodetic and seismic observations when combined with appropriate slip-rate functions. We compute volumetric stress tensor changes c_{ij} resulting from this imposed slip distribution on the megathrust interface using SeisSol in a dynamic relaxation calculation [121, 123], utilizing the same computational mesh and slab geometry as in our subsequent dynamic rupture simulations. We impose a regularized Yoffe slip-rate function as an internal boundary condition to compute the stress changes across the slab interface. This approach leverages the discontinuous finite-element discretization of SeisSol, accurately capturing displacement discontinuities along the fault interface. We perform dynamic relaxation for 200 seconds, sufficient for all seismic waves to exit the computational domain and achieve steady-state stress conditions. In contrast to previous methods, which used finite-fault slip models primarily to estimate fault-interface stresses [e.g., 124–127], our calculation simultaneously estimates both fault-interface and surrounding volumetric stress changes. High slip gradients can lead to unrealistic stress concentrations, particularly in shallow regions. To mitigate this, we include inelastic off-fault plastic yielding during the dynamic relaxation step, employing the same parameters as during dynamic rupture simulations (Section “Off-fault plasticity”). The resulting stress changes on the megathrust interface are shown in Supplementary Fig. S3.

Grid search for initial stress and fault strength

To systematically explore effects of dynamically viable initial stress and fault strength conditions on rupture evolution, we conduct a grid search [128] across a range of stress heterogeneity amplitudes (α) and regional relative prestress levels (R_0) (Fig. 6). We vary α from 1.0 to 1.2 in increments of 0.01, and R_0 from 0.1 to 0.2 in increments of 0.005 to generate 33 sets of parameters for simulating spontaneous earthquake rupture. Each model is evaluated based on comparisons between its outputs and the observed moment magnitude, moment-rate functions, and both onshore and offshore geodetic displacements [60, 129–132] (Supplementary Fig. S5). Out of this set of dynamic rupture scenarios, we identify a preferred model that best matches observations (Fig. 2).

Regional stress rupture model without stress heterogeneity

When only using the regionally constrained stress tensor b_{ij} (i.e., $\alpha = 0$), we obtain a laterally homogeneous prestress model with a uniform relative prestress ratio R across the entire megathrust (Fig. 1b, Extended Fig. E1a). This homogeneity results from the principal stress orientations and overall geometry of the Japan subduction zone being largely uniform along strike. To systematically explore dynamic rupture scenarios without imposed stress heterogeneity, we vary the regional relative prestress level R_0 within the range 0.56–0.64 in increments of 0.02, consistent with the average relative prestress value within the rupture area of the preferred model (Fig. 1d).

In all five homogeneous stress scenarios, dynamic rupture propagates along the entire megathrust interface. The rupture model with $R_0 = 0.58$ yields an unrealistic magnitude of M_w 9.61 and an extended rupture duration of 180 s (Extended Fig. E7). In contrast to the preferred model, the laterally homogeneous prestress model exhibits crack-like rupture reactivation (Extended Fig. E8, Supplementary Fig S6 and Video S2), occurring at the downdip healing front of the growing pulse. This simulation does not reproduce the distinct updip and downdip rupture propagation speeds and complex rupture evolution documented in back-projection studies [6, 133–135] (Extended Fig. E8b).

Breakdown work density

Breakdown work is defined as the frictional work that provides an estimate of the irreversible part of the total strain energy change, which does not go into radiated energy [37]. The breakdown work combines fracture energy and restrengthening work [125, 136, 137]. Since multiple rupture episodes occur during most of our simulations, we sum the breakdown work of each rupture episode into the total breakdown work W_b (red-shaded areas in Extended Fig. E4). We then define the breakdown work density W'_b per unit area, defined as the excess of work over the minimum shear stress level achieved during total slip:

$$W'_b = \int_0^{t_f} (\tau(t) - \tau_{min}) \dot{\delta}(t) dt, \quad (23)$$

where $\dot{\delta}(t)$ is the slip velocity and t_f is the end time of the rupture defined as the absolute slip-rate decrease less than $0.01 m/s$. The calculated breakdown work density of the preferred model is shown in Extended Fig. E6. The breakdown work density exhibits significant spatial variability and depends on the rupture process [138]. Multiple slip pulses downdip and in the hypocentral region generally increase the breakdown work density, compared to updip regions. The average breakdown work density of the preferred model is $19.6 MJ/m^2$, consistent with the estimated and expected average breakdown work density for an M_w 9 event [7, 87, 136].

Extended Data

Table E1: Fault frictional properties assumed in this study. VW: velocity-weakening, VS: velocity-strengthening.

Parameter	Symbol	Values	Unit
Direct-effect parameter	a	VW: 0.01 VS: 0.018	
Evolution-effect parameter	b	0.014	
Reference slip rate	V_0	10^{-6}	m/s
Steady-state low-velocity friction coefficient at slip rate V_0	f_0	0.5	
Weakened slip rate	V_W	0.1	m/s
State evolution distance [†]	L	0.6	m
Fully weakened friction coefficient	f_w	0.1	
Initial slip velocity	V_i	10^{-16}	m/s

[†] State evolution distance L is initially set to 0.2m within 6 km radius of the hypocenter location, increases linearly to 0.6 m within a 12 km radius, and remains constant of 0.6 m elsewhere. (See Supplementary Section “SM2: Nucleation” for details)

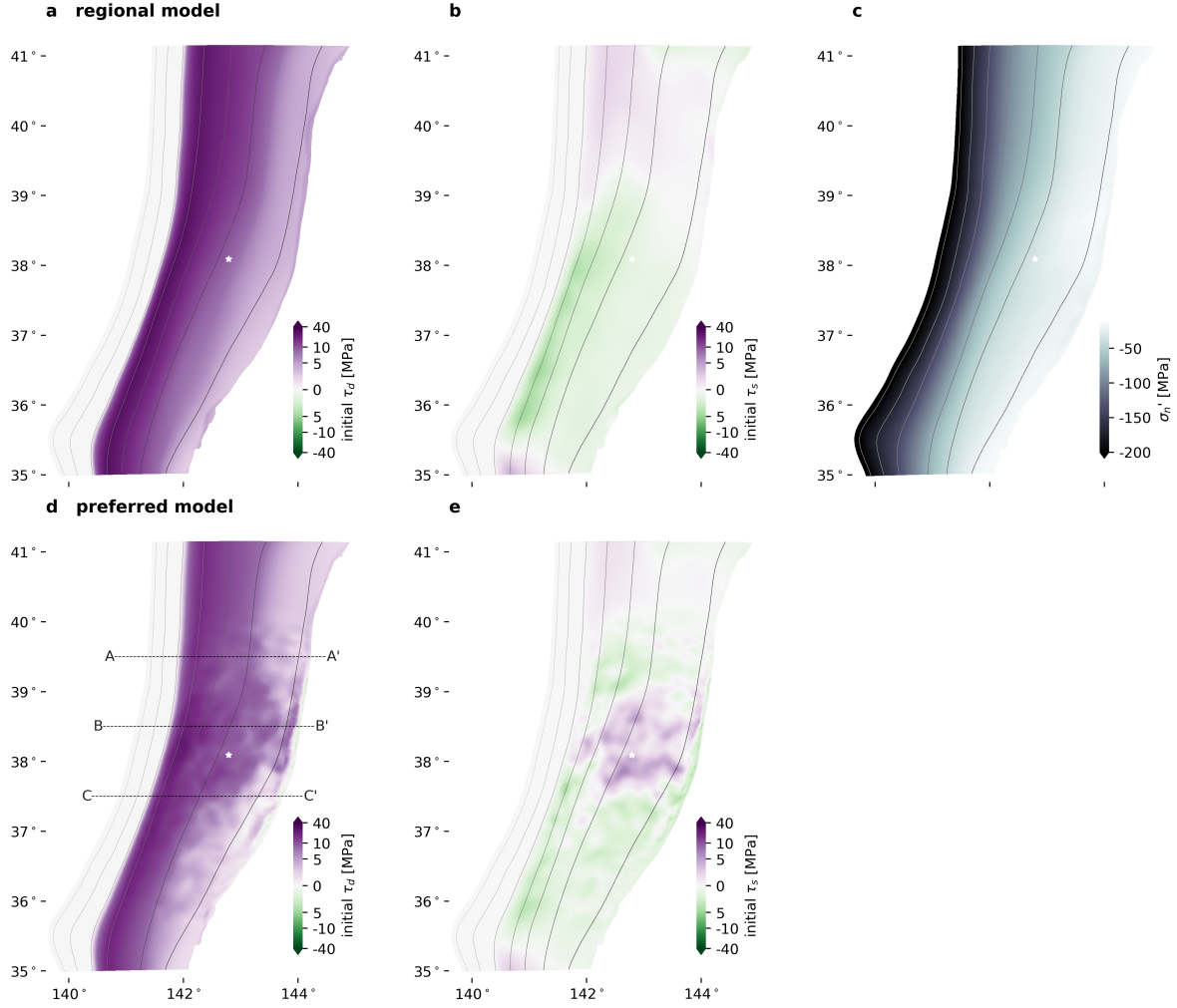


Figure E1: Initial shear stress and effective normal stress distribution along the megathrust interface. (a, b) Initial shear stress (τ_d , τ_s) distribution for the homogeneous regional stress dynamic rupture model (shown in Fig. 1b). (c) Depth-dependent distribution of effective normal stress (σ'_n). (d, e) Initial shear stress distribution for the preferred model incorporating stress heterogeneity from the median finite-fault model in Wong *et al.* [12]. Hypocenter location (star) and depth contours (gray lines, 10 km intervals) are shown in all panels.

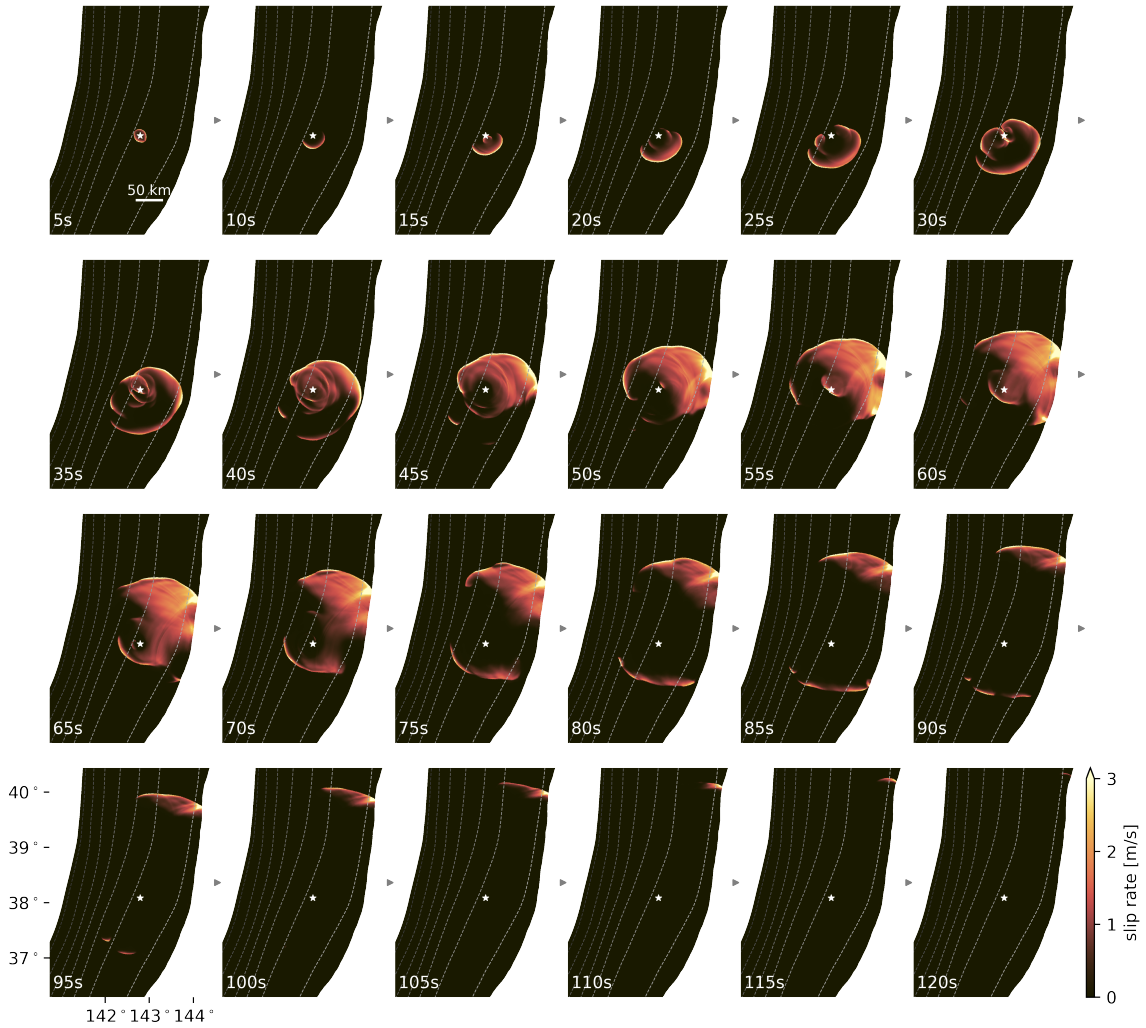


Figure E2: Dynamic rupture evolution of the preferred model. Snapshots of slip rate shown in 5 s intervals, see also Supplementary Video S1. Earthquake rupture initiates as a growing pulse within the first 15 s, followed by a first rupture reactivation initiating at the primary pulse' healing front between 15–25 s. Between 25–40 s, reactivated rupture fronts coalesce, “spiral” and back-propagate, resulting in complex slip rate patterns and a second major hypocentral slip reactivation at 40 s, taking again the form of a growing pulse. Between 40 s and 50 s rupture time, the primary updip rupture front reaches the seafloor interface, resulting in strong dynamic interactions with the free surface and generating reflected phases. The third episode of hypocentral rupture reactivation occurs at around 50 s, initiating at the healing front of the secondary propagating pulse-like rupture. A fourth reactivated pulse emerging at 65 s is not sustained. Subsequently, after around 75 s, the rupture simplifies and propagates pulse-like bilaterally along strike, featuring extended shallow rupture in the northern portion of the megathrust between 100–120 s, consistent with slip models inferred from tsunami inversion studies [51, 139, 140]. The white star denotes the hypocenter location.

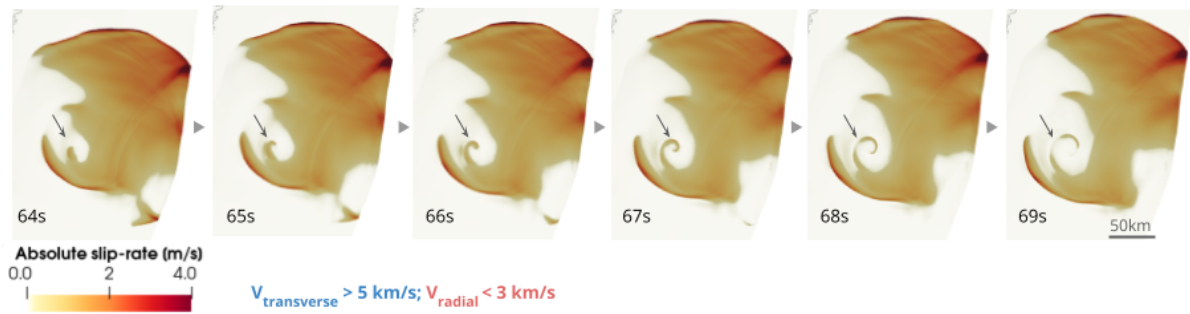


Figure E3: Rapid transverse expansion of a circular rupture front, resembling recent laboratory observations [42]. Snapshots show slip rate evolution of a circular, spiraling rupture front from 64 s to 69 s. The black arrows mark the onset location where the circular rupture front forms. The spiraling rupture reaches a radius of approximately 12 km from the hypocenter and sweeps a 180° arc within 5 s. Its rupture speed exceeds 7 km/s, which is higher than the local shear wave speed at the corresponding depth of ≈ 20 km (Supplementary Table S1).

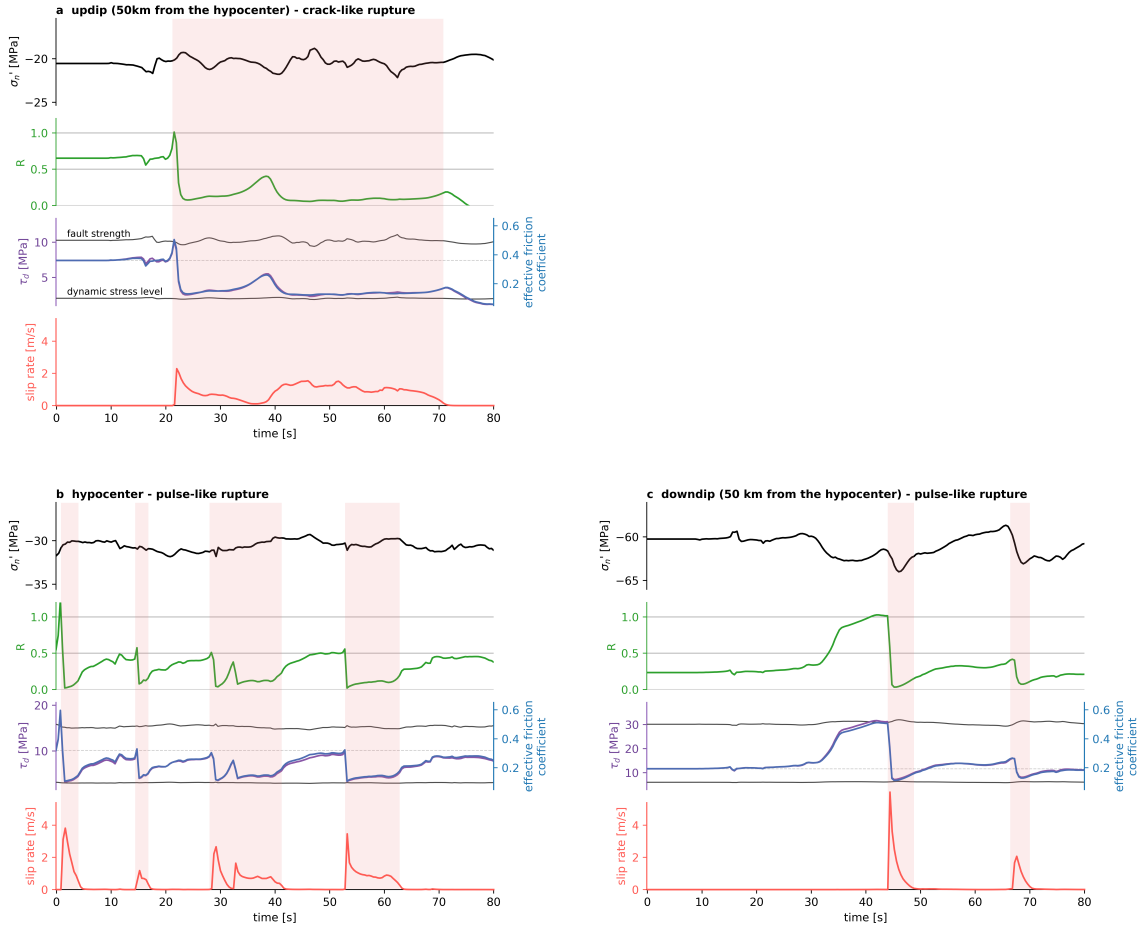


Figure E4: Temporal evolution of effective normal stress σ'_n (black), relative prestress level R (green), along-dip shear stress τ_d (purple), effective friction coefficient (blue), and slip rate (red) of the preferred model. (a) Evolution in the updip, (b) hypocentral, and (c) downdip regions. The shaded red areas denote periods when the slip rate exceeds 0.05 m/s. In the along-dip shear stress panels, the light gray dashed lines represent the initial shear stress, while the solid black lines indicate the fault strength ($f_0\sigma'_n$) and dynamic stress level ($f_w\sigma'_n$).

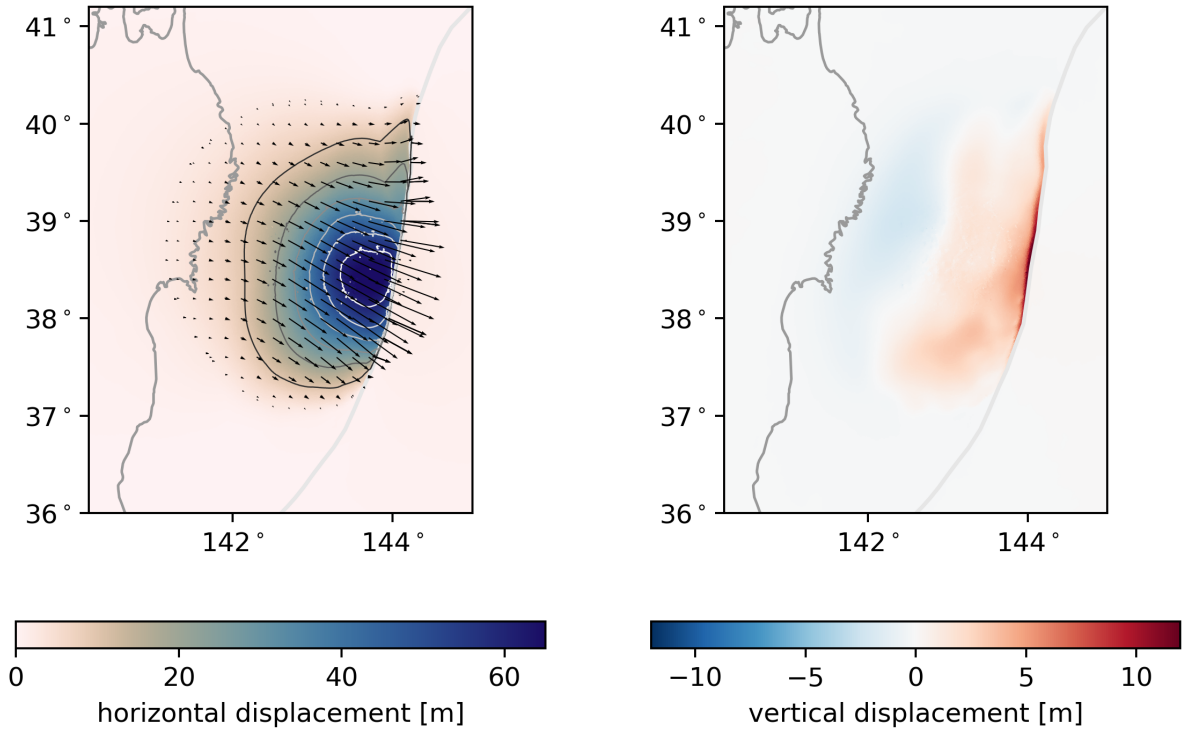


Figure E5: Simulated seafloor displacement from the preferred dynamic rupture model. (a) Horizontal and (b) vertical displacement fields. In (a), contours show horizontal displacement amplitudes at 10 m intervals, the gray line denotes the trench location. The near-trench modeled horizontal and vertical displacements are broadly consistent with differential bathymetry observations [9, 47, 49, 141, 142]. The pronounced uplift in the northern near-trench region (in b) agrees with deformation inferred from tsunami waveform inversion [51, 139, 140, 143, 144].

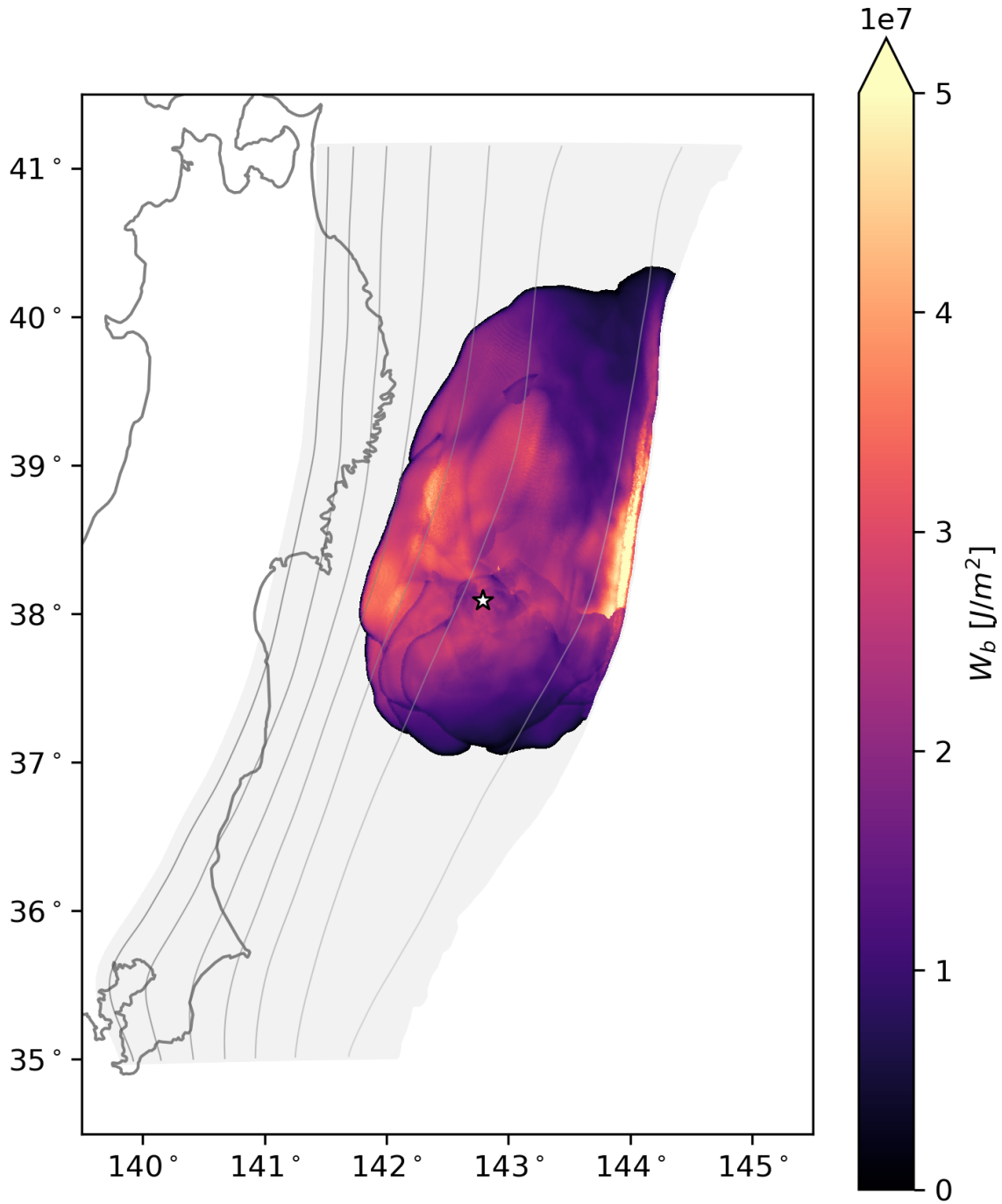


Figure E6: Breakdown work density (W'_b , Methods Sec. Breakdown work density) distribution for the preferred dynamic rupture model. The preferred model shows pronounced spatial variation in breakdown work density, where downdip slip pulses increase the breakdown work density, compared to the updip region.

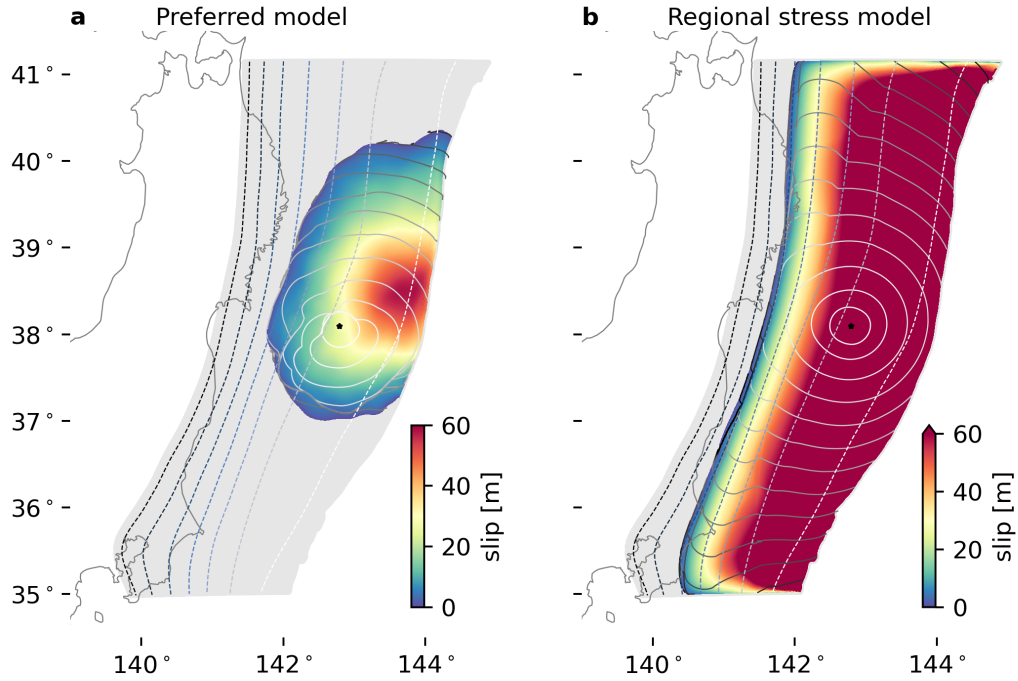


Figure E7: Comparison of fault slip distribution and rupture evolution between (a) the heterogeneous prestress model (the preferred model) and (b) the laterally homogeneous prestress model. Solid contour lines indicate rupture front location at 10 s intervals. The preferred model spontaneously arrests with $M_w=8.96$, whereas the laterally homogeneous prestress model fails to arrest and ruptures the entire fault, reaching $M_w=9.61$. Depth contours (dotted lines, 10 km intervals) and the hypocenter location (star, [40]) are shown in both panels.

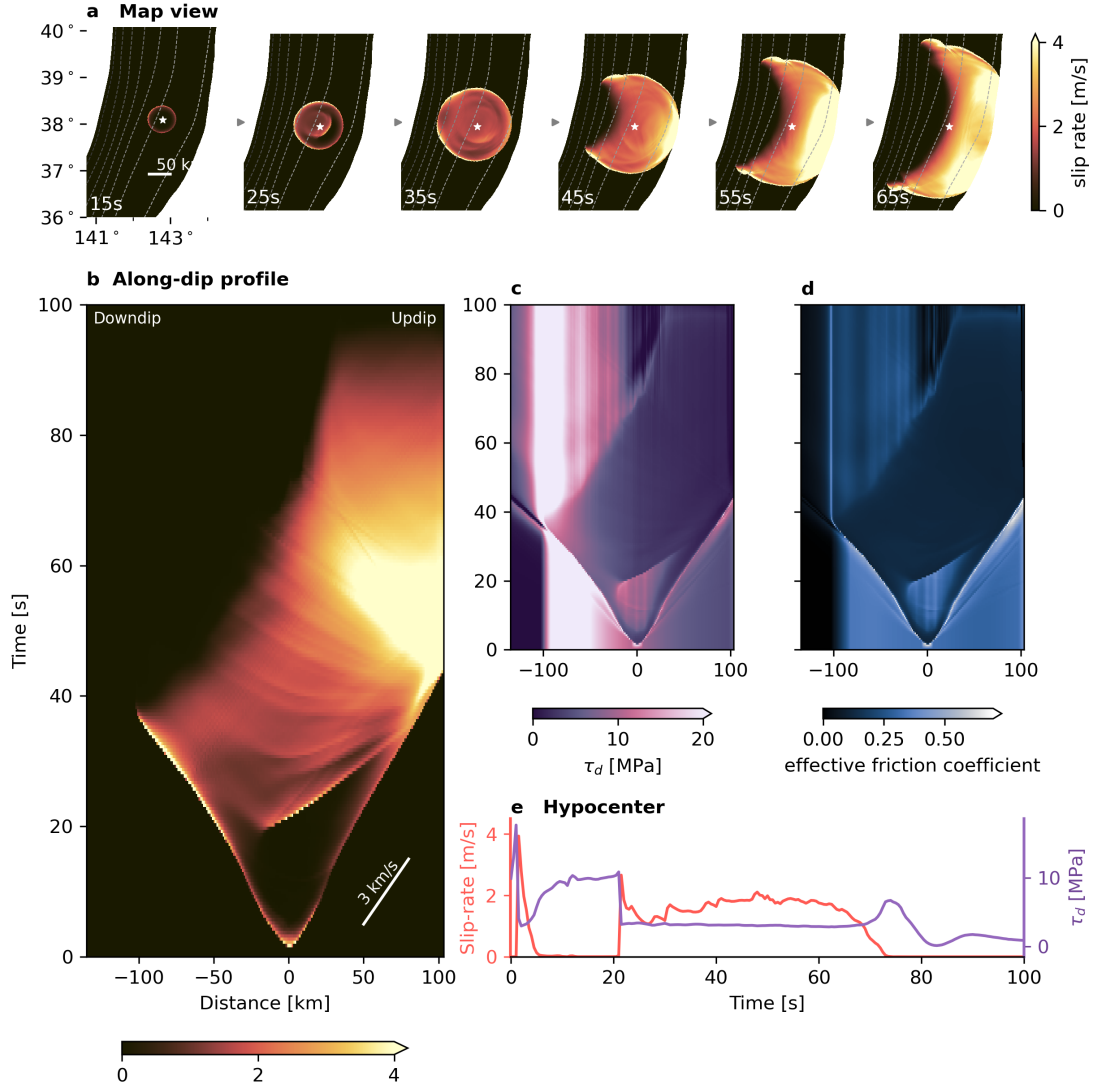


Figure E8: Rupture dynamics of the laterally homogeneous prestress model, see also Supplementary Fig. S6 and Supplementary Video S2. (a) Map-view snapshots of slip rate evolution at 10 s intervals. A primary growing pulse is followed by crack-like slip reactivation at approximately 20 s, propagating updip. Primary and secondary rupture fronts subsequently merge into sustained crack-like rupture without clear healing fronts distinguishing separate slip episodes. The white star indicates the hypocenter location. (b)-(d) Temporal evolution of slip rate, along-dip shear stress τ_d (purple), and effective friction coefficient (blue) along a hypocentral dip profile, highlighting rapid coseismic restrengthening and subsequent rupture reactivation. (e) Time series of hypocentral slip rate (red) and along-dip shear stress τ_d (purple).

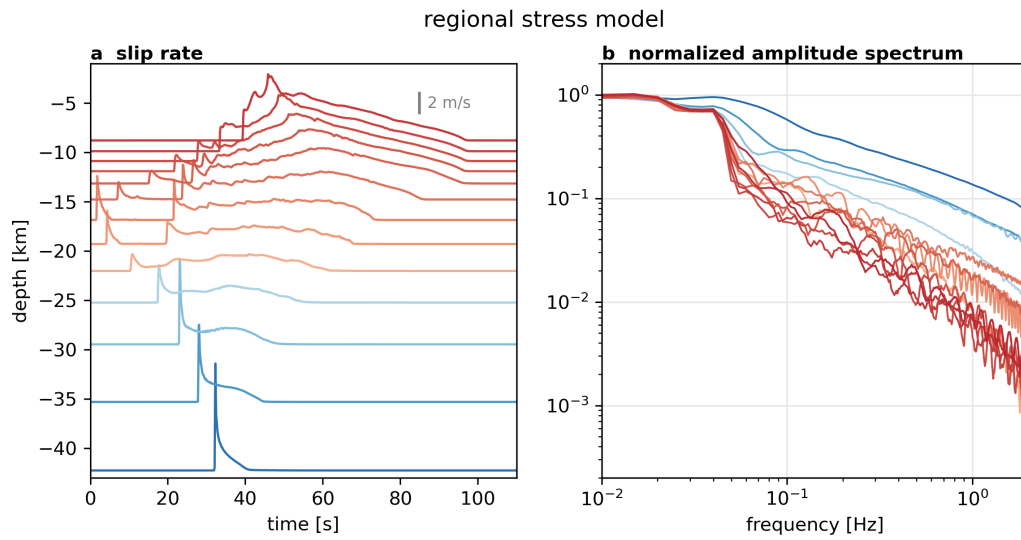


Figure E9: Depth-dependent slip rate characteristics in the laterally homogeneous prestress model. (a) Slip rate functions along-dip through the hypocenter at various depths. Down-dip pulse-like ruptures are highlighted in blue, while up-dip crack-like ruptures are indicated in red. (b) Normalized amplitude spectra of the corresponding slip rate functions shown in (a), illustrating distinct frequency content between down-dip pulse-like and up-dip crack-like rupture styles.

References

1. Wirth, E. A., Sahakian, V. J., Wallace, L. M. & Melnick, D. The Occurrence and Hazards of Great Subduction Zone Earthquakes. *Nature Reviews Earth & Environment* **3**, 125–140. doi:10.1038/s43017-021-00245-w (2022).
2. Uchida, N. & Bürgmann, R. A Decade of Lessons Learned from the 2011 Tohoku-Oki Earthquake. *Reviews of Geophysics* **59**, e2020RG000713. doi:10.1029/2020RG000713 (2021).
3. Lee, S.-J., Huang, B.-S., Ando, M., Chiu, H.-C. & Wang, J.-H. Evidence of Large Scale Repeating Slip during the 2011 Tohoku-Oki Earthquake: REPEATING SLIP DURING TOHOKU EARTHQUAKE. *Geophysical Research Letters* **38**, n/a–n/a. doi:10.1029/2011GL049580 (2011).
4. Ide, S., Baltay, A. & Beroza, G. C. Shallow Dynamic Overshoot and Energetic Deep Rupture in the 2011 M_w 9.0 Tohoku-Oki Earthquake. *Science* **332**, 1426–1429. doi:10.1126/science.1207020 (2011).
5. Melgar, D. & Bock, Y. Kinematic Earthquake Source Inversion and Tsunami Runup Prediction with Regional Geophysical Data. *Journal of Geophysical Research: Solid Earth* **120**, 3324–3349. doi:10.1002/2014JB011832 (2015).
6. Meng, L., Inbal, A. & Ampuero, J.-P. A Window into the Complexity of the Dynamic Rupture of the 2011 Mw 9 Tohoku-Oki Earthquake: THE 2011 TOHOKU-OKI EARTHQUAKE. *Geophysical Research Letters* **38**, n/a–n/a. doi:10.1029/2011GL048118 (2011).
7. Lay, T. *et al.* Depth-Varying Rupture Properties of Subduction Zone Megathrust Faults. *Journal of Geophysical Research: Solid Earth* **117**. doi:10.1029/2011JB009133 (2012).
8. Fujiwara, T. *et al.* The 2011 Tohoku-Oki Earthquake: Displacement Reaching the Trench Axis. *Science* **334**, 1240–1240. doi:10.1126/science.1211554 (2011).
9. Kodaira, S., Fujiwara, T., Fujie, G., Nakamura, Y. & Kanamatsu, T. Large Coseismic Slip to the Trench During the 2011 Tohoku-Oki Earthquake. *Annual Review of Earth and Planetary Sciences* **48**, 321–343. doi:10.1146/annurev-earth-071719-055216 (2020).
10. Wallace, L., Cochran, U., Power, W. & Clark, K. Earthquake and Tsunami Potential of the Hikurangi Subduction Thrust, New Zealand: Insights from Paleoseismology, GPS, and Tsunami Modeling. *Oceanography* **27**, 104–117. doi:10.5670/oceanog.2014.46 (2014).

11. Frankel, A., Wirth, E., Marafi, N., Vidale, J. & Stephenson, W. Broadband Synthetic Seismograms for Magnitude 9 Earthquakes on the Cascadia Megathrust Based on 3D Simulations and Stochastic Synthetics, Part 1: Methodology and Overall Results. *Bulletin of the Seismological Society of America* **108**, 2347–2369. doi:10.1785/0120180034 (2018).
12. Wong, J. W. C., Fan, W. & Gabriel, A.-A. A Quantitative Comparison and Validation of Finite-Fault Models: The 2011 Tohoku-Oki Earthquake. *Journal of Geophysical Research: Solid Earth* **129**, e2024JB029212. doi:10.1029/2024JB029212 (2024).
13. Huang, Y., Ampuero, J.-P. & Kanamori, H. Slip-Weakening Models of the 2011 Tohoku-Oki Earthquake and Constraints on Stress Drop and Fracture Energy. *Pure and Applied Geophysics* **171**, 2555–2568. doi:10.1007/s00024-013-0718-2 (2014).
14. Galvez, P., Petukhin, A., Irikura, K. & Somerville, P. Dynamic Source Model for the 2011 Tohoku Earthquake in a Wide Period Range Combining Slip Reactivation with the Short-Period Ground Motion Generation Process. *Pure and Applied Geophysics* **177**, 2143–2161. doi:10.1007/s00024-019-02210-7 (2020).
15. Ma, S. Wedge Plasticity and a Minimalist Dynamic Rupture Model for the 2011 MW 9.1 Tohoku-Oki Earthquake and Tsunami. *Tectonophysics* **869**, 230146. doi:10.1016/j.tecto.2023.230146 (2023).
16. Ampuero, J.-P. & Rubin, A. M. Earthquake Nucleation on Rate and State Faults – Aging and Slip Laws. *Journal of Geophysical Research: Solid Earth* **113**, 2007JB005082. doi:10.1029/2007JB005082 (2008).
17. Ke, C.-Y., McLaskey, G. C. & Kammer, D. S. Rupture Termination in Laboratory-Generated Earthquakes. *Geophysical Research Letters* **45**. doi:10.1029/2018GL080492 (2018).
18. Lambert, V., Lapusta, N. & Perry, S. Propagation of Large Earthquakes as Self-Healing Pulses or Mild Cracks. *Nature* **591**, 252–258. doi:10.1038/s41586-021-03248-1 (2021).
19. Dieterich, J. H. Modeling of Rock Friction: 1. Experimental Results and Constitutive Equations. *Journal of Geophysical Research: Solid Earth* **84**, 2161–2168. doi:10.1029/JB084iB05p02161 (1979).
20. Ruina, A. Slip Instability and State Variable Friction Laws. *Journal of Geophysical Research: Solid Earth* **88**, 10359–10370. doi:10.1029/JB088iB12p10359 (1983).
21. Noda, H., Dunham, E. M. & Rice, J. R. Earthquake Ruptures with Thermal Weakening and the Operation of Major Faults at Low Overall Stress Levels. *Journal of Geophysical Research: Solid Earth* **114**, 2008JB006143. doi:10.1029/2008JB006143 (2009).
22. Di Toro, G. *et al.* Fault Lubrication during Earthquakes. *Nature* **471**, 494–498. doi:10.1038/nature09838 (2011).

23. Ujiie, K. *et al.* Low Coseismic Shear Stress on the Tohoku-Oki Megathrust Determined from Laboratory Experiments. *Science* **342**, 1211–1214. doi:10.1126/science.1243485 (2013).
24. Xia, K., Rosakis, A. J. & Kanamori, H. Laboratory Earthquakes: The Sub-Rayleigh-to-Supershear Rupture Transition. *Science* **303**, 1859–1861. doi:10.1126/science.1094022 (2004).
25. Gabriel, A.-A., Ampuero, J.-P., Dalguer, L. A. & Mai, P. M. The Transition of Dynamic Rupture Styles in Elastic Media under Velocity-Weakening Friction. *Journal of Geophysical Research: Solid Earth* **117**. doi:10.1029/2012JB009468 (2012).
26. Ulrich, T., Gabriel, A.-A., Ampuero, J.-P. & Xu, W. Dynamic Viability of the 2016 Mw 7.8 Kaikōura Earthquake Cascade on Weak Crustal Faults. *Nature Communications* **10**, 1213. doi:10.1038/s41467-019-09125-w (2019).
27. Rubino, V., Lapusta, N. & Rosakis, A. J. Intermittent Lab Earthquakes in Dynamically Weakening Fault Gouge. *Nature* **606**, 922–929. doi:10.1038/s41586-022-04749-3 (2022).
28. Lapusta, N. & Rice, J. R. Nucleation and Early Seismic Propagation of Small and Large Events in a Crustal Earthquake Model. *Journal of Geophysical Research: Solid Earth* **108**, 2001JB000793. doi:10.1029/2001JB000793 (2003).
29. Cattania, C. Complex Earthquake Sequences On Simple Faults. *Geophysical Research Letters* **46**, 10384–10393. doi:10.1029/2019GL083628 (2019).
30. Barbot, S. Slow-Slip, Slow Earthquakes, Period-Two Cycles, Full and Partial Ruptures, and Deterministic Chaos in a Single Asperity Fault. *Tectonophysics* **768**, 228171. doi:10.1016/j.tecto.2019.228171 (2019).
31. Heidbach, O. *et al.* The World Stress Map database release 2016: Crustal stress pattern across scales. *Tectonophysics* **744**, 484–498 (2018).
32. Uphoff, C. *et al.* Extreme Scale Multi-Physics Simulations of the Tsunamigenic 2004 Sumatra Megathrust Earthquake in *Proceedings of the International Conference for High Performance Computing, Networking, Storage and Analysis* (ACM, Denver Colorado, 2017), 1–16. doi:10.1145/3126908.3126948.
33. Hok, S., Fukuyama, E. & Hashimoto, C. Dynamic Rupture Scenarios of Anticipated Nankai-Tonankai Earthquakes, Southwest Japan. *Journal of Geophysical Research* **116**, B12319. doi:10.1029/2011JB008492 (2011).
34. Kozdon, J. E. & Dunham, E. M. Rupture to the Trench: Dynamic Rupture Simulations of the 11 March 2011 Tohoku Earthquake. *Bulletin of the Seismological Society of America* **103**, 1275–1289. doi:10.1785/0120120136 (2013).
35. Ulrich, T., Gabriel, A.-A. & Madden, E. H. Stress, Rigidity and Sediment Strength Control Megathrust Earthquake and Tsunami Dynamics. *Nature Geoscience* **15**, 67–73. doi:10.1038/s41561-021-00863-5 (2022).

36. Saffer, D. M. & Marone, C. Comparison of Smectite- and Illite-Rich Gouge Frictional Properties: Application to the Updip Limit of the Seismogenic Zone along Subduction Megathrusts. *Earth and Planetary Science Letters* **215**, 219–235. doi:10.1016/S0012-821X(03)00424-2 (2003).
37. Kammer, D. S. *et al.* Earthquake Energy Dissipation in a Fracture Mechanics Framework. *Nature Communications* **15**, 4736. doi:10.1038/s41467-024-47970-6 (2024).
38. Yagi, Y. & Fukahata, Y. Rupture Process of the 2011 Tohoku-oki Earthquake and Absolute Elastic Strain Release. *Geophysical Research Letters* **38**, n/a–n/a. doi:10.1029/2011GL048701 (2011).
39. Brown, L., Wang, K. & Sun, T. Static Stress Drop in the M_w 9 Tohoku-oki Earthquake: Heterogeneous Distribution and Low Average Value. *Geophysical Research Letters* **42**. doi:10.1002/2015GL066361 (2015).
40. Hayes, G. P. Rapid Source Characterization of the 2011 M_w 9.0 off the Pacific Coast of Tohoku Earthquake. *Earth, Planets and Space* **63**, 529–534. doi:10.5047/eps.2011.05.012 (2011).
41. Valli, M. A New Database of Source Time Functions (STFs) Extracted from the SCARDEC Method. *Physics of the Earth and Planetary Interiors* (2016).
42. Cochard, T. *et al.* Propagation of Extended Fractures by Local Nucleation and Rapid Transverse Expansion of Crack-Front Distortion. *Nature Physics* **20**, 660–665. doi:10.1038/s41567-023-02365-0 (2024).
43. Sun, Y. & Cattania, C. Back-propagating Earthquakes on a Simple Fault. *Authorea Preprints*. doi:10.22541/essoar.173724475.50020741/v1 (2025).
44. Nielsen, S. & Madariaga, R. On the Self-Healing Fracture Mode. *Bulletin of the Seismological Society of America* **93**, 2375–2388. doi:10.1785/0120020090 (2003).
45. Kurahashi, S. & Irikura, K. Short-Period Source Model of the 2011 M_w 9.0 Off the Pacific Coast of Tohoku Earthquake. *Bulletin of the Seismological Society of America* **103**, 1373–1393. doi:10.1785/0120120157 (2013).
46. Heaton, T. H. Evidence for and Implications of Self-Healing Pulses of Slip in Earthquake Rupture. *Physics of the Earth and Planetary Interiors* **64**, 1–20. doi:10.1016/0031-9201(90)90002-F (1990).
47. Ueda, H. *et al.* The Submarine Fault Scarp of the 2011 Tohoku-oki Earthquake in the Japan Trench. *Communications Earth & Environment* **4**, 476. doi:10.1038/s43247-023-01118-4 (2023).
48. Loveless, J. P. & Meade, B. J. Two Decades of Spatiotemporal Variations in Subduction Zone Coupling Offshore Japan. *Earth and Planetary Science Letters* **436**, 19–30. doi:10.1016/j.epsl.2015.12.033 (2016).

49. Zhang, K. *et al.* Complex Tsunamigenic Near-Trench Seafloor Deformation during the 2011 Tohoku–Oki Earthquake. *Nature Communications* **14**, 3260. doi:10.1038/s41467-023-38970-z (2023).
50. Barras, F., Thøgersen, K., Aharonov, E. & Renard, F. How Do Earthquakes Stop? Insights From a Minimal Model of Frictional Rupture. *Journal of Geophysical Research: Solid Earth* **128**, e2022JB026070. doi:10.1029/2022JB026070 (2023).
51. Satake, K., Fujii, Y., Harada, T. & Namegaya, Y. Time and Space Distribution of Coseismic Slip of the 2011 Tohoku Earthquake as Inferred from Tsunami Waveform Data. *Bulletin of the Seismological Society of America* **103**, 1473–1492. doi:10.1785/0120120122 (2013).
52. Das, S. & Aki, K. A Numerical Study of Two-Dimensional Spontaneous Rupture Propagation. *Geophysical Journal International* **50**, 643–668. doi:10.1111/j.1365-246X.1977.tb01339.x (1977).
53. Zheng, G. & Rice, J. R. Conditions under Which Velocity-Weakening Friction Allows a Self-Healing versus a Cracklike Mode of Rupture. *Bulletin of the Seismological Society of America* **88**, 1466–1483. doi:10.1785/BSSA0880061466 (1998).
54. Kammer, D. S., Radiguet, M., Ampuero, J.-P. & Molinari, J.-F. Linear Elastic Fracture Mechanics Predicts the Propagation Distance of Frictional Slip. *Tribology Letters* **57**, 23. doi:10.1007/s11249-014-0451-8 (2015).
55. Moore, J. C., Plank, T. A., Chester, F. M., Polissar, P. J. & Savage, H. M. Sediment Provenance and Controls on Slip Propagation: Lessons Learned from the 2011 Tohoku and Other Great Earthquakes of the Subducting Northwest Pacific Plate. *Geosphere* **11**, 533–541. doi:10.1130/GES01099.1 (2015).
56. Tsuru, T. *et al.* Along-Arc Structural Variation of the Plate Boundary at the Japan Trench Margin: Implication of Interplate Coupling. *Journal of Geophysical Research: Solid Earth* **107**, ESE 11-1–ESE 11-15. doi:10.1029/2001JB001664 (2002).
57. Bassett, D. & Watts, A. B. Gravity Anomalies, Crustal Structure, and Seismicity at Subduction Zones: 2. Interrelationships between Fore-Arc Structure and Seismogenic Behavior. *Geochemistry, Geophysics, Geosystems* **16**, 1541–1576. doi:10.1002/2014GC005685 (2015).
58. Okuwaki, R., Yagi, Y. & Hirano, S. Relationship between High-frequency Radiation and Asperity Ruptures, Revealed by Hybrid Back-projection with a Non-planar Fault Model. *Scientific Reports* **4**, 7120. doi:10.1038/srep07120 (2014).
59. Vallée, M. *et al.* Self-Reactivated Rupture during the 2019 M = 8 Northern Peru Intralab Earthquake. *Earth and Planetary Science Letters* **601**, 117886. doi:10.1016/j.epsl.2022.117886 (2023).
60. Sagiya, T. A decade of GEONET: 1994-2003 The continuous GPS observation in Japan and its impact on earthquake studies. *Earth, planets and space* **56**, xxix–xli (2004).

61. Oeser, J., Bunge, H.-P. & Mohr, M. *Cluster design in the earth sciences tethys in International conference on high performance computing and communications* (2006), 31–40.
62. Yao, S. & Yang, H. Rupture Dynamics of the 2012 Nicoya M_w 7.6 Earthquake: Evidence for Low Strength on the Megathrust. *Geophysical Research Letters* **47**, e2020GL087508. doi:10.1029/2020GL087508 (2020).
63. Ramos, M. D. *et al.* Assessing Margin-Wide Rupture Behaviors Along the Cascadia Megathrust With 3-D Dynamic Rupture Simulations. *Journal of Geophysical Research: Solid Earth* **126**, e2021JB022005. doi:10.1029/2021JB022005 (2021).
64. Chan, Y. P. B., Yao, S. & Yang, H. Impact of Hypocenter Location on Rupture Extent and Ground Motion: A Case Study of Southern Cascadia. *Journal of Geophysical Research: Solid Earth* **128**, e2023JB026371. doi:10.1029/2023JB026371 (2023).
65. Wirp, S. A., Gabriel, A.-A., Ulrich, T. & Lorito, S. Dynamic Rupture Modeling of Large Earthquake Scenarios at the Hellenic Arc Toward Physics-Based Seismic and Tsunami Hazard Assessment. *Journal of Geophysical Research: Solid Earth* **129**, e2024JB029320. doi:10.1029/2024JB029320 (2024).
66. Li, D. & Gabriel, A.-A. Linking 3D Long-Term Slow-Slip Cycle Models With Rupture Dynamics: The Nucleation of the 2014 Mw 7.3 Guerrero, Mexico Earthquake. *AGU Advances* **5**, e2023AV000979. doi:10.1029/2023AV000979 (2024).
67. Duan, B. Dynamic Rupture of the 2011 Mw 9.0 Tohoku-Oki Earthquake: Roles of a Possible Subducting Seamount. *Journal of Geophysical Research: Solid Earth* **117**. doi:10.1029/2011JB009124 (2012).
68. Ide, S. & Aochi, H. Historical Seismicity and Dynamic Rupture Process of the 2011 Tohoku-Oki Earthquake. *Tectonophysics. Great Earthquakes along Subduction Zones* **600**, 1–13. doi:10.1016/j.tecto.2012.10.018 (2013).
69. Dumbser, M. & Käser, M. An Arbitrary High-Order Discontinuous Galerkin Method for Elastic Waves on Unstructured Meshes — II. The Three-Dimensional Isotropic Case. *Geophysical Journal International* **167**, 319–336. doi:10.1111/j.1365-246X.2006.03120.x (2006).
70. Heinecke, A. *et al.* *Petascale High Order Dynamic Rupture Earthquake Simulations on Heterogeneous Supercomputers in SC '14: Proceedings of the International Conference for High Performance Computing, Networking, Storage and Analysis* ISSN: 2167-4337 (2014), 3–14. doi:10.1109/SC.2014.6. <https://ieeexplore.ieee.org/document/7012188> (2024).
71. Krenz, L. *et al.* *3D Acoustic-Elastic Coupling with Gravity: The Dynamics of the 2018 Palu, Sulawesi Earthquake and Tsunami in Proceedings of the International Conference for High Performance Computing, Networking, Storage and Analysis* (ACM, St. Louis Missouri, 2021), 1–14. doi:10.1145/3458817.3476173.

72. Pelties, C., de la Puente, J., Ampuero, J.-P., Brietzke, G. B. & Käser, M. Three-Dimensional Dynamic Rupture Simulation with a High-Order Discontinuous Galerkin Method on Unstructured Tetrahedral Meshes. *Journal of Geophysical Research: Solid Earth* **117**. doi:10.1029/2011JB008857 (2012).
73. Pelties, C., Gabriel, A.-A. & Ampuero, J.-P. Verification of an ADER-DG Method for Complex Dynamic Rupture Problems. *Geoscientific Model Development* **7**, 847–866. doi:10.5194/gmd-7-847-2014 (2014).
74. Harris, R. A. *et al.* A Suite of Exercises for Verifying Dynamic Earthquake Rupture Codes. *Seismological Research Letters* **89**, 1146–1162. doi:10.1785/0220170222 (2018).
75. Taufiqurrahman, T., Gabriel, A.-A., Ulrich, T., Valentová, L. & Gallovič, F. Broadband Dynamic Rupture Modeling With Fractal Fault Roughness, Frictional Heterogeneity, Viscoelasticity and Topography: The 2016 M_w 6.2 Amatrice, Italy Earthquake. *Geophysical Research Letters* **49**, e2022GL098872. doi:10.1029/2022GL098872 (2022).
76. Breuer, A. & Heinecke, A. *Next-Generation Local Time Stepping for the ADER-DG Finite Element Method* in 2022 IEEE International Parallel and Distributed Processing Symposium (IPDPS) (IEEE, Lyon, France, 2022), 402–413. doi:10.1109/IPDPS53621.2022.00046.
77. Koketsu, K., Miyake, H., Tanaka, Y., *et al.* A proposal for a standard procedure of modeling 3-D velocity structures and its application to the Tokyo metropolitan area, Japan. *Tectonophysics* **472**, 290–300 (2009).
78. Koketsu, K., Miyake, H. & Suzuki, H. *Japan integrated velocity structure model version 1* in *Proceedings of the 15th world conference on earthquake engineering* **1** (2012), 4.
79. Group, G. C. *GEBCO 2024 Grid* 2024. doi:doi : 10.5285/1c44ce99-0a0d-5f4f-e063-7086abc0ea0f.
80. Fukuyama, E. Automated seismic moment tensor determination by using on-line broadband seismic waveforms [in Japanese with English abstract]. *J. Seismol. Soc. Jpn.* **51**, 149 (1998).
81. Day, S. M., Dalguer, L. A., Lapusta, N. & Liu, Y. Comparison of Finite Difference and Boundary Integral Solutions to Three-Dimensional Spontaneous Rupture. *Journal of Geophysical Research: Solid Earth* **110**. doi:10.1029/2005JB003813 (2005).
82. Goldsby, D. L. & Tullis, T. E. Flash Heating Leads to Low Frictional Strength of Crustal Rocks at Earthquake Slip Rates. *Science* **334**, 216–218. doi:10.1126/science.1207902 (2011).
83. Brodsky, E. E. *et al.* The State of Stress on the Fault Before, During, and After a Major Earthquake. *Annual Review of Earth and Planetary Sciences* **48**, 49–74. doi:10.1146/annurev-earth-053018-060507 (2020).

84. Rice, J. R. Heating and Weakening of Faults during Earthquake Slip. *Journal of Geophysical Research: Solid Earth* **111**. doi:10.1029/2005JB004006 (2006).
85. Beeler, N. M., Tullis, T. E. & Goldsby, D. L. Constitutive Relationships and Physical Basis of Fault Strength Due to Flash Heating. *Journal of Geophysical Research: Solid Earth* **113**. doi:10.1029/2007JB004988 (2008).
86. Ujiie, K. & Tsutsumi, A. High-Velocity Frictional Properties of Clay-Rich Fault Gouge in a Megasplay Fault Zone, Nankai Subduction Zone. *Geophysical Research Letters* **37**. doi:10.1029/2010GL046002 (2010).
87. Viesca, R. C. & Garagash, D. I. Ubiquitous Weakening of Faults Due to Thermal Pressurization. *Nature Geoscience* **8**, 875–879. doi:10.1038/ngeo2554 (2015).
88. Bizzarri, A. & Cocco, M. A Thermal Pressurization Model for the Spontaneous Dynamic Rupture Propagation on a Three-dimensional Fault: 1. Methodological Approach. *Journal of Geophysical Research: Solid Earth* **111**, 2005JB003862. doi:10.1029/2005JB003862 (2006).
89. Noda, H. & Lapusta, N. Stable Creeping Fault Segments Can Become Destructive as a Result of Dynamic Weakening. *Nature* **493**, 518–521. doi:10.1038/nature11703 (2013).
90. Schmitt, S. V., Segall, P. & Dunham, E. M. Nucleation and Dynamic Rupture on Weakly Stressed Faults Sustained by Thermal Pressurization. *Journal of Geophysical Research: Solid Earth* **120**, 7606–7640. doi:10.1002/2015JB012322 (2015).
91. Wang, Y. & Day, S. M. Seismic Source Spectral Properties of Crack-like and Pulse-like Modes of Dynamic Rupture. *Journal of Geophysical Research: Solid Earth* **122**, 6657–6684. doi:10.1002/2017JB014454 (2017).
92. Perry, S. M., Lambert, V. & Lapusta, N. Nearly Magnitude-Invariant Stress Drops in Simulated Crack-Like Earthquake Sequences on Rate-and-State Faults with Thermal Pressurization of Pore Fluids. *Journal of Geophysical Research: Solid Earth* **125**, e2019JB018597. doi:10.1029/2019JB018597 (2020).
93. Palgunadi, K. H., Gabriel, A.-A., Garagash, D. I., Ulrich, T. & Mai, P. M. Rupture Dynamics of Cascading Earthquakes in a Multiscale Fracture Network. *Journal of Geophysical Research: Solid Earth* **129**, e2023JB027578. doi:10.1029/2023JB027578 (2024).
94. Fulton, P. M. *et al.* Low Coseismic Friction on the Tohoku-Oki Fault Determined from Temperature Measurements. *Science* **342**, 1214–1217. doi:10.1126/science.1243641 (2013).
95. Dunham, E. M., Belanger, D., Cong, L. & Kozdon, J. E. Earthquake Ruptures with Strongly Rate-Weakening Friction and Off-Fault Plasticity, Part 1: Planar Faults. *Bulletin of the Seismological Society of America* **101**, 2296–2307. doi:10.1785/0120100075 (2011).

96. Lambert, V. & Lapusta, N. Absolute Stress Levels in Models of Low-Heat Faults: Links to Geophysical Observables and Differences for Crack-like Ruptures and Self-Healing Pulses. *Earth and Planetary Science Letters* **618**, 118277. doi:10.1016/j.epsl.2023.118277 (2023).
97. Premus, J., Gallovič, F. & Ampuero, J.-P. Bridging Time Scales of Faulting: From Co-seismic to Postseismic Slip of the Mw 6.0 2014 South Napa, California Earthquake. *Science Advances* **8**, eabq2536. doi:10.1126/sciadv.abq2536 (2022).
98. Dieterich, J. H. & Kilgore, B. D. Direct Observation of Frictional Contacts: New Insights for State-Dependent Properties. *Pure and Applied Geophysics PAGEOPH* **143**, 283–302. doi:10.1007/BF00874332 (1994).
99. Dieterich, J. H. Earthquake Nucleation on Faults with Rate-and State-Dependent Strength. *Tectonophysics* **211**, 115–134. doi:10.1016/0040-1951(92)90055-B (1992).
100. Ikari, M. J. & Kopf, A. J. Cohesive Strength of Clay-Rich Sediment. *Geophysical Research Letters* **38**. doi:10.1029/2011GL047918 (2011).
101. Ikari, M. J., Kameda, J., Saffer, D. M. & Kopf, A. J. Strength Characteristics of Japan Trench Borehole Samples in the High-Slip Region of the 2011 Tohoku-Oki Earthquake. *Earth and Planetary Science Letters* **412**, 35–41. doi:10.1016/j.epsl.2014.12.014 (2015).
102. Nishikawa, T. *et al.* The Slow Earthquake Spectrum in the Japan Trench Illuminated by the S-net Seafloor Observatories. *Science* **365**, 808–813. doi:10.1126/science.aax5618 (2019).
103. Nishikawa, T., Ide, S. & Nishimura, T. A Review on Slow Earthquakes in the Japan Trench. *Progress in Earth and Planetary Science* **10**, 1. doi:10.1186/s40645-022-00528-w (2023).
104. Madden, E. H., Ulrich, T. & Gabriel, A.-A. The State of Pore Fluid Pressure and 3-D Megathrust Earthquake Dynamics. *Journal of Geophysical Research: Solid Earth* **127**, e2021JB023382. doi:10.1029/2021JB023382 (2022).
105. Saffer, D. M. & Tobin, H. J. Hydrogeology and Mechanics of Subduction Zone Forearcs: Fluid Flow and Pore Pressure. *Annual Review of Earth and Planetary Sciences* **39**, 157–186. doi:10.1146/annurev-earth-040610-133408 (2011).
106. Jamali Hondori, E. & Park, J.-O. Connection between High Pore-Fluid Pressure and Frictional Instability at Tsunamigenic Plate Boundary Fault of 2011 Tohoku-Oki Earthquake. *Scientific Reports* **12**, 12556. doi:10.1038/s41598-022-16578-5 (2022).
107. Hardebeck, J. L. & Loveless, J. P. Creeping Subduction Zones Are Weaker than Locked Subduction Zones. *Nature Geoscience* **11**, 60–64. doi:10.1038/s41561-017-0032-1 (2018).

108. Andrews, D. J. Rupture Dynamics with Energy Loss Outside the Slip Zone. *Journal of Geophysical Research: Solid Earth* **110**. doi:10.1029/2004JB003191 (2005).
109. Wollherr, S., Gabriel, A.-A. & Uphoff, C. Off-Fault Plasticity in Three-Dimensional Dynamic Rupture Simulations Using a Modal Discontinuous Galerkin Method on Unstructured Meshes: Implementation, Verification and Application. *Geophysical Journal International* **214**, 1556–1584. doi:10.1093/gji/ggy213 (2018).
110. Templeton, E. L. & Rice, J. R. Off-Fault Plasticity and Earthquake Rupture Dynamics: 1. Dry Materials or Neglect of Fluid Pressure Changes. *Journal of Geophysical Research: Solid Earth* **113**. doi:10.1029/2007JB005529 (2008).
111. Gabriel, A.-A., Ampuero, J.-P., Dalguer, L. A. & Mai, P. M. Source Properties of Dynamic Rupture Pulses with Off-fault Plasticity. *Journal of Geophysical Research: Solid Earth* **118**, 4117–4126. doi:10.1002/jgrb.50213 (2013).
112. Ma, S. A Physical Model for Widespread Near-Surface and Fault Zone Damage Induced by Earthquakes. *Geochemistry, Geophysics, Geosystems* **9**. doi:10.1029/2008GC002231 (2008).
113. Ma, S. & Nie, S. Dynamic Wedge Failure and Along-Arc Variations of Tsunamigenesis in the Japan Trench Margin. *Geophysical Research Letters* **46**, 8782–8790. doi:10.1029/2019GL083148 (2019).
114. Nielsen, S. B. & Carlson, J. M. Rupture Pulse Characterization: Self-Healing, Self-Similar, Expanding Solutions in a Continuum Model of Fault Dynamics. *Bulletin of the Seismological Society of America* **90**, 1480–1497. doi:10.1785/0120000021 (2000).
115. Gallovič, F., Valentová, Ľ., Ampuero, J.-P. & Gabriel, A.-A. Bayesian Dynamic Finite-Fault Inversion: 1. Method and Synthetic Test. *Journal of Geophysical Research: Solid Earth* **124**, 6949–6969. doi:10.1029/2019JB017510 (2019).
116. Galvez, P., Ampuero, J.-P., Dalguer, L. A., Somala, S. N. & Nissen-Meyer, T. Dynamic Earthquake Rupture Modelled with an Unstructured 3-D Spectral Element Method Applied to the 2011 M₉ Tohoku Earthquake. *Geophysical Journal International* **198**, 1222–1240. doi:10.1093/gji/ggu203 (2014).
117. Galvez, P., Dalguer, L. A., Ampuero, J.-P. & Giardini, D. Rupture Reactivation during the 2011 M_w 9.0 Tohoku Earthquake: Dynamic Rupture and Ground-Motion Simulations. *Bulletin of the Seismological Society of America* **106**, 819–831. doi:10.1785/0120150153 (2016).
118. Huang, Y., Meng, L. & Ampuero, J.-P. A Dynamic Model of the Frequency-Dependent Rupture Process of the 2011 Tohoku-Oki Earthquake. *Earth, Planets and Space* **64**, 1061–1066. doi:10.5047/eps.2012.05.011 (2012).

119. Jia, Z. *et al.* The Complex Dynamics of the 2023 Kahramanmaraş, Turkey, M_w 7.8–7.7 Earthquake Doublet. *Science* **381**, 985–990. doi:10.1126/science.adf0685 (2023).
120. Hayek, J. N. *et al.* Non-Typical Supershear Rupture: Fault Heterogeneity and Segmentation Govern Unilateral Supershear and Cascading Multi-Fault Rupture in the 2021 M_w 7.4 Maduo Earthquake. *Geophysical Research Letters* **51**, e2024GL110128. doi:10.1029/2024GL110128 (2024).
121. Tinti, E. *et al.* Constraining Families of Dynamic Models Using Geological, Geodetic and Strong Ground Motion Data: The M_w 6.5, October 30th, 2016, Norcia Earthquake, Italy. *Earth and Planetary Science Letters* **576** (2021).
122. Aochi, H. The 1999 Izmit, Turkey, Earthquake: Nonplanar Fault Structure, Dynamic Rupture Process, and Strong Ground Motion. *Bulletin of the Seismological Society of America* **93**, 1249–1266. doi:10.1785/0120020167 (2003).
123. Glehman, J. *et al.* Partial Ruptures Governed by the Complex Interplay between Geodetic Slip Deficit, Rigidity, and Pore Fluid Pressure in 3D Cascadia Dynamic Rupture Simulations (2024).
124. Day, S. M., Yu, G. & Wald, D. J. Dynamic stress changes during earthquake rupture. *Bulletin of the Seismological Society of America* **88**, 512–522. doi:10.1785/BSSA0880020512 (1998).
125. Tinti, E., Spudich, P. & Cocco, M. Earthquake Fracture Energy Inferred from Kinematic Rupture Models on Extended Faults. *Journal of Geophysical Research: Solid Earth* **110**, 2005JB003644. doi:10.1029/2005JB003644 (2005).
126. Causse, M., Dalguer, L. A. & Mai, P. M. Variability of dynamic source parameters inferred from kinematic models of past earthquakes. *Geophysical Journal International* **196**, 1754–1769. doi:10.1093/gji/ggt478 (2014).
127. Yang, H., Yao, S., He, B. & Newman, A. V. Earthquake rupture dependence on hypocentral location along the Nicoya Peninsula subduction megathrust. *Earth and Planetary Science Letters* **520**, 10–17. doi:https://doi.org/10.1016/j.epsl.2019.05.030 (2019).
128. Weng, H. & Yang, H. Constraining Frictional Properties on Fault by Dynamic Rupture Simulations and Near-Field Observations. *Journal of Geophysical Research: Solid Earth* **123**, 6658–6670. doi:10.1029/2017JB015414 (2018).
129. Ito, T., Ozawa, K., Watanabe, T. & Sagiya, T. Slip Distribution of the 2011 off the Pacific Coast of Tohoku Earthquake Inferred from Geodetic Data. *Earth, Planets and Space* **63**, 627–630. doi:10.5047/eps.2011.06.023 (2011).

130. Kido, M., Osada, Y., Fujimoto, H., Hino, R. & Ito, Y. Trench-Normal Variation in Observed Seafloor Displacements Associated with the 2011 Tohoku-Oki Earthquake: SEAFLOOR MOVEMENT OF TOHOKU EARTHQUAKE. *Geophysical Research Letters* **38**, n/a–n/a. doi:10.1029/2011GL050057 (2011).
131. Sato, M. *et al.* Displacement Above the Hypocenter of the 2011 Tohoku-Oki Earthquake. *Science* **332**, 1395–1395. doi:10.1126/science.1207401 (2011).
132. Yokota, Y., Ishikawa, T. & Watanabe, S.-i. Seafloor Crustal Deformation Data along the Subduction Zones around Japan Obtained by GNSS-A Observations. *Scientific Data* **5**, 180182. doi:10.1038/sdata.2018.182 (2018).
133. Koper, K. D., Hutko, A. R. & Lay, T. Along-Dip Variation of Teleseismic Short-Period Radiation from the 11 March 2011 Tohoku Earthquake (Mw 9.0). *Geophysical Research Letters* **38**. doi:10.1029/2011GL049689 (2011).
134. Yagi, Y., Nakao, A. & Kasahara, A. Smooth and Rapid Slip near the Japan Trench during the 2011 Tohoku-oki Earthquake Revealed by a Hybrid Back-Projection Method. *Earth and Planetary Science Letters* **355–356**, 94–101. doi:10.1016/j.epsl.2012.08.018 (2012).
135. Yao, H., Shearer, P. M. & Gerstoft, P. Compressive Sensing of Frequency-Dependent Seismic Radiation from Subduction Zone Megathrust Ruptures. *Proceedings of the National Academy of Sciences* **110**, 4512–4517. doi:10.1073/pnas.1212790110 (2013).
136. Cocco, M. *et al.* Fracture Energy and Breakdown Work During Earthquakes. *Annual Review of Earth and Planetary Sciences* **51**, 217–252. doi:10.1146/annurev-earth-071822-100304 (2023).
137. Gabriel, A.-A., Garagash, D. I., Palgunadi, K. H. & Mai, P. M. Fault Size-Dependent Fracture Energy Explains Multiscale Seismicity and Cascading Earthquakes. *Science* **385**, eadj9587. doi:10.1126/science.adj9587 (2024).
138. Lambert, V. & Lapusta, N. Rupture-Dependent Breakdown Energy in Fault Models with Thermo-Hydro-Mechanical Processes. *Solid Earth* **11**, 2283–2302. doi:10.5194/se-11-2283-2020 (2020).
139. Yamazaki, Y., Cheung, K. F. & Lay, T. A Self-Consistent Fault Slip Model for the 2011 Tohoku Earthquake and Tsunami. *Journal of Geophysical Research: Solid Earth* **123**, 1435–1458. doi:10.1002/2017JB014749 (2018).
140. Kubota, T., Saito, T. & Hino, R. A New Mechanical Perspective on a Shallow Megathrust Near-Trench Slip from the High-Resolution Fault Model of the 2011 Tohoku-Oki Earthquake. *Progress in Earth and Planetary Science* **9**, 68. doi:10.1186/s40645-022-00524-0 (2022).

141. Fujii, Y., Satake, K., Sakai, S., Shinohara, M. & Kanazawa, T. Tsunami Source of the 2011 off the Pacific Coast of Tohoku Earthquake. *Earth, Planets and Space* **63**, 815–820. doi:10.5047/eps.2011.06.010 (2011).
142. Sun, T., Wang, K., Fujiwara, T., Kodaira, S. & He, J. Large Fault Slip Peaking at Trench in the 2011 Tohoku-oki Earthquake. *Nature Communications* **8**, 14044. doi:10.1038/ncomms14044 (2017).
143. Hossen, M. J., Cummins, P. R., Dettmer, J. & Baba, T. Tsunami Waveform Inversion for Sea Surface Displacement Following the 2011 Tohoku Earthquake: Importance of Dispersion and Source Kinematics. *Journal of Geophysical Research: Solid Earth* **120**, 6452–6473. doi:10.1002/2015JB011942 (2015).
144. Dettmer, J. *et al.* Tsunami Source Uncertainty Estimation: The 2011 Japan Tsunami. *Journal of Geophysical Research: Solid Earth* **121**, 4483–4505. doi:10.1002/2015JB012764 (2016).
145. Käser, M. & Dumbser, M. An Arbitrary High-Order Discontinuous Galerkin Method for Elastic Waves on Unstructured Meshes — I. The Two-Dimensional Isotropic Case with External Source Terms. *Geophysical Journal International* **166**, 855–877. doi:10.1111/j.1365-246X.2006.03051.x (2006).
146. Lay, T., Ammon, C. J., Kanamori, H., Xue, L. & Kim, M. J. Possible Large Near-Trench Slip during the 2011 M_w 9.0 off the Pacific Coast of Tohoku Earthquake. *Earth, Planets and Space* **63**, 687–692. doi:10.5047/eps.2011.05.033 (2011).
147. Ide, S. Estimation of Radiated Energy of Finite-Source Earthquake Models. *Bulletin of the Seismological Society of America* **92**, 2994–3005. doi:10.1785/0120020028 (2002).
148. Aochi, H. & Ide, S. Conceptual Multi-Scale Dynamic Rupture Model for the 2011 off the Pacific Coast of Tohoku Earthquake. *Earth, Planets and Space* **63**, 761–765. doi:10.5047/eps.2011.05.008 (2011).
149. Lay, T. A Review of the Rupture Characteristics of the 2011 Tohoku-oki Mw 9.1 Earthquake. *Tectonophysics* **733**, 4–36. doi:10.1016/j.tecto.2017.09.022 (2018).
150. Wang, K. *et al.* Learning from Crustal Deformation Associated with the M9 2011 Tohoku-oki Earthquake. *Geosphere* **14**, 552–571. doi:10.1130/GES01531.1 (2018).
151. Andrews, D. J. Rupture Velocity of Plane Strain Shear Cracks. *Journal of Geophysical Research* **81**, 5679–5687. doi:10.1029/JB081i032p05679 (1976).
152. Hu, F., Oglesby, D. D. & Chen, X. The Sustainability of Free-Surface-Induced Supershear Rupture on Strike-Slip Faults. *Geophysical Research Letters* **46**, 9537–9543. doi:10.1029/2019GL084318 (2019).

Supplementary Information

Supplementary datasets

Supplementary video S1: Evolution of slip rate (left), along-dip shear stress τ_d (center), and effective friction coefficient (right) of the preferred dynamic rupture model.

Supplementary video S2: Evolution of slip rate (left), along-dip shear stress τ_d (center), and effective friction coefficient (right) of the laterally homogeneous prestress model.

Supplementary video S3: Evolution of slip rate (left), along-dip shear stress τ_d (center), and effective friction coefficient (right) of the simple reactivation rupture model shown in Fig 6c.

SM1: Model resolution

Numerical convergence of dynamic rupture simulations is governed by the resolution of the process zone [81]. We follow Wollherr *et al.* [109] to determine the required on-fault resolution of our SeisSol dynamic rupture simulations, which use basis functions of polynomial order $p = 5$. Our mesh features an element size of 1000 m everywhere along the slab. This ensures that we resolve the average process zone width, which we measure to be $\Lambda=4,500$ m in our preferred model.

Off-the slab, we employ a velocity-aware adaptive mesh refinement approach [76], focusing resolution along the slab interface and in onshore regions. The target frequency resolved by the mesh is determined by:

$$f \approx V_s / (\Delta x \times \text{elements per wavelength}), \quad (24)$$

with Δx defining the tetrahedral element size, V_s as the S wave speed. We follow the analysis by [145] and require at least two elements per wavelength, suitable for polynomial basis functions of order $p = 5$ in space and time. While our mesh is conservatively designed to resolve seismic wave propagation throughout the domain at frequencies up to 1 Hz, it resolves seismic wavefields recorded at seismic stations at frequencies up to 2 Hz (Supplementary Fig. S8).

SM2: Nucleation

The Tohoku-Oki earthquake began with a low initial moment-release rate [40, 41, 146], which is challenging to capture in dynamic rupture simulations that cannot account for long-term fault slip evolution. Our models capture the slow initiation behavior using a smooth nucleation procedure and scale-dependent fracture energy in the hypocentral region [137, 147, 148].

Following common practice from community dynamic rupture benchmarks [74], we define an overstressed nucleation region with a radius of r_{nuc} of 7 km and an additional shear stress

perturbation of 10 MPa to locally reach the yielding stress level. We position the nucleation patch at the hypocenter location provided by the USGS (142.7897°E, 38.0919°N) [40]. The stress perturbation is smoothly imposed spatially and temporally, using an exponential spatial function $f(r)$ and a smooth temporal function $g(t)$:

$$f(r) = \exp[r^2/(r^2 - r_{crit}^2)], \quad (25)$$

$$g(t) = \exp[(t - T)^2/t(t - 2T)], \quad (26)$$

with $T = 3s$.

To ensure a realistic, gradual rupture initiation, we impose a spatially variable slip-weakening distance [35]. The state evolution distance is set to $L = 0.2$ m within a 6 km radius from the hypocenter, increases linearly to 0.6 m within a 12 km radius, and remains constant at $L = 0.6$ m and beyond. To quantify the effects of varying slip-weakening distances, we perform an additional simulation using a uniform slip-weakening distance of 0.3 m. This uniform nucleation model reproduces the overall dynamic complexity seen in our preferred model, including multiple rupture reactivation, depth-dependent rupture characteristics, substantial slip to the trench, and spontaneous rupture arrest (Supplementary Fig. S7). However, it results in the peak slip rate being reached early, at 50 s. This dynamic rupture model also does not match the geodetic deformation as closely as our preferred model, with an onshore and offshore geodetic data variance reduction of 76.1% and 34.1%, respectively.

SM3: Dynamic stress drop

To quantify the modeled spatially varying dynamic stress drop ($\Delta\tau$), defined as the difference between initial and final shear stresses during the rupture, we compute the slip-weighted mean stress drop across the ruptured area:

$$\Delta\sigma_E = \frac{\int_{\Sigma} \Delta\tau \delta dS}{\int_{\Sigma} \delta dS}, \quad (27)$$

where Σ is the rupture area and δ denotes the slip amplitude. Our preferred rupture model yields a slip-weighted average dynamic stress drop of 2.37 MPa, comparable to the estimated stress drop of finite-fault slip models [39].

Table S1: 1D velocity model, modified from [80]

Depth[km]	Thickness [km]	P-wave velocity [km/s]	S-wave velocity [km/s]	Density [kg/m^3]
3	3	5.5	3.14	2300
18	15	6.0	3.55	2400
33	15	6.7	3.84	2800
100	67	7.8	4.46	3200
∞	∞	8.0	4.57	3300

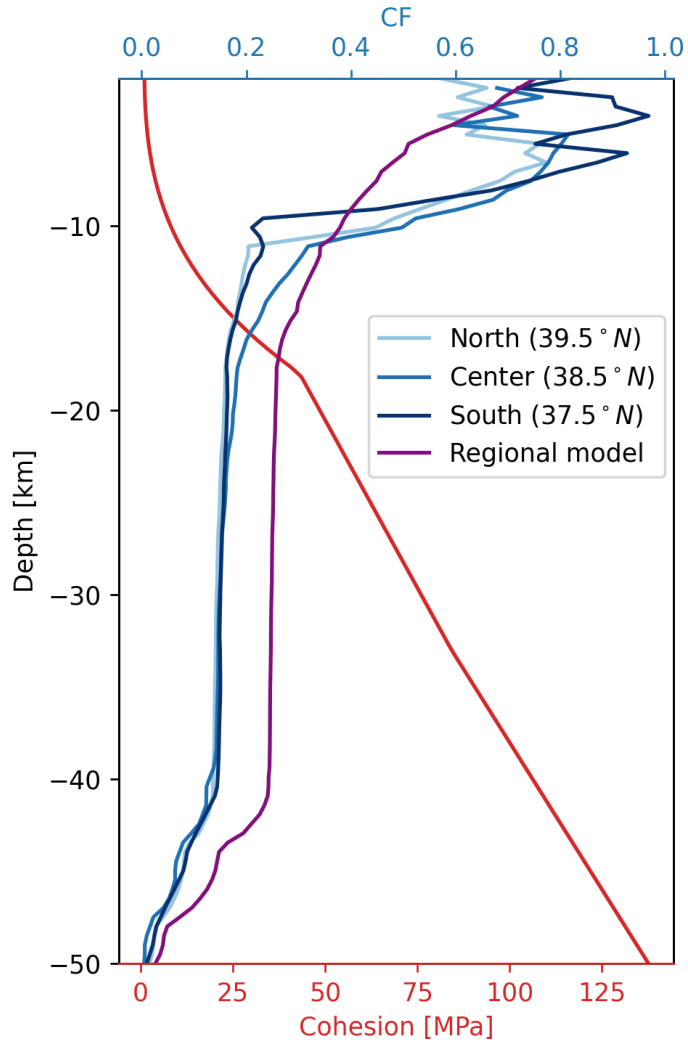


Figure S1: Depth-dependent cohesion (red) and closeness-to-failure (CF) profiles across the north (light blue), center (blue), and south (dark blue) cross sections as of Fig 5 of the preferred model, and the laterally homogeneous prestress model (purple). See Methods Sec. “Off-fault plasticity”.

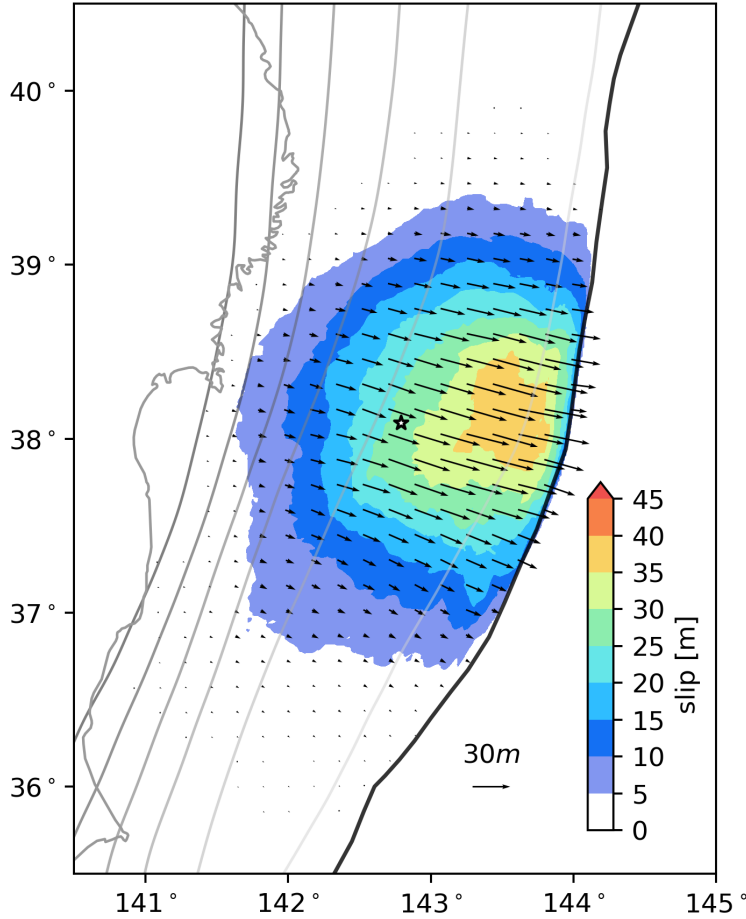


Figure S2: Median slip distribution computed from 32 finite-fault slip distributions of the Tohoku-Oki earthquake compiled by [12] and projected onto our new slab geometry (Methods Sec. ‘Model geometry and mesh’). Colors and vectors represent the amplitude and direction of slip. Gray contour lines indicate the slab geometry at 10 km depth intervals. The USGS hypocenter is indicated as the star [40]. The median slip model reveals a smoothly distributed circular slip patch predominantly updip from the hypocenter, confined mostly along strike. Large slip extends toward the trench, reaching a maximum amplitude of approximately 38.0 m roughly 5 km away from the trench axis. This major slip feature has been recognized in [2, 149, 150], although previous discussions have been largely qualitative.

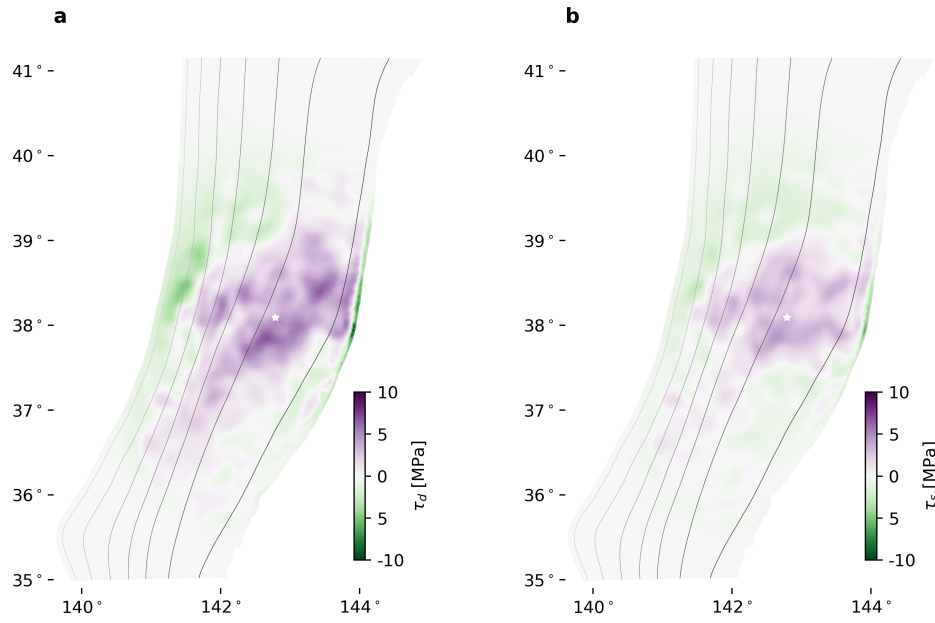


Figure S3: Stress changes resulting from the median finite-fault slip distribution on the megathrust interface. (a) Along-dip shear stress change. (b) Along-strike shear stress change. These stress changes serve as the basis for constructing the observationally informed initial stress conditions for dynamic rupture modeling.

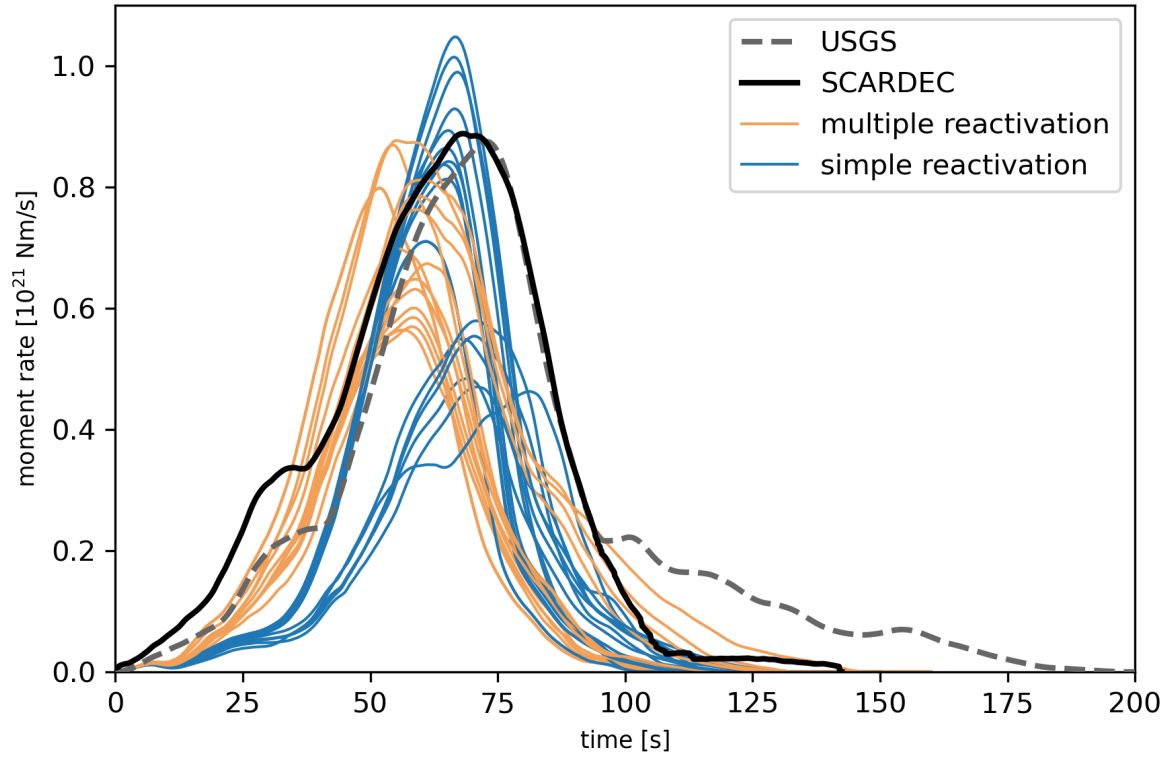


Figure S4: Comparison of moment-rate functions for two distinct rupture styles shown in Figure 6. Yellow lines represent the moment-rate functions of dynamic rupture models characterized by repeated rupture reactivation near the hypocenter, while blue lines correspond to models dominated by single pulse-like ruptures with free-surface reflection. The reactivation model captures the early moment-rate evolution within the first 40 s, while the simple reactivation rupture model underestimates moment release during the 0–40 s rupture time interval.

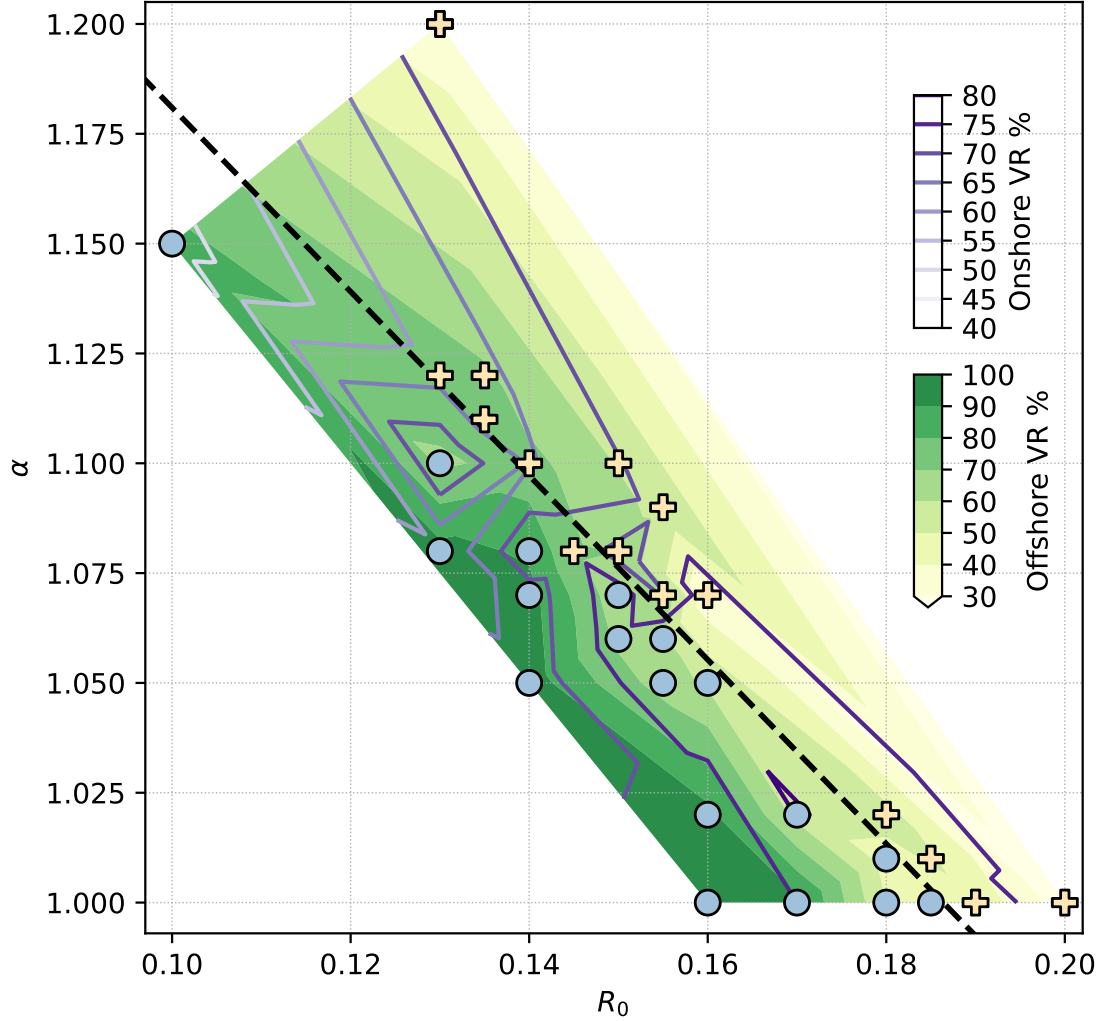


Figure S5: Comparison of onshore and offshore geodetic displacement misfits across models with varying prestress heterogeneity amplitude (α) and regional ambient stress level R_0 . Green-filled contours indicate variance reduction for offshore geodetic data, while purple contour lines represent variance reduction for onshore data. Blue circles represent a family of dynamic rupture models dominated by single pulse-like ruptures driven by free-surface reflection, while yellow crosses denote models exhibiting repeated rupture reactivation near the hypocenter. Our results illustrate that stress heterogeneity amplitude (α) primarily controls peak slip magnitude, whereas the regional relative stress level R_0 predominantly determines rupture extent.



Figure S6: Dynamic rupture evolution of the laterally homogeneous prestress model (see also Fig. E8 and Supplementary Video S2). Snapshots of slip rate are shown in 5 s intervals. Earthquake rupture initiates as a growing pulse, followed by rupture reactivation initiating at the downdip healing front of the primary growing pulse at 20 s. Between 20–40 s, primary and secondary rupture fronts subsequently merge into a sustained, crack-like rupture without clear healing fronts separating slip episodes. At 40 s, rupture reaches the downdip limit of the seismogenic zone, forming a healing front that propagates updip and progressively shortens central slip rise times toward shallower depths as the rupture expands along strike. At the same time, bilateral deep supershear rupture is initiated ahead of the primary rupture front via the “daughter crack” mechanism [151] and likely due to higher effective normal stress and a relatively sharp transition to velocity-strengthening friction at depth [152]. This local supershear rupture remains confined to depths between 30–50 km. At 45 s rupture time, about 5 s later compared to the preferred model, the primary updip rupture front reaches the seafloor interface, resulting in reflected phases. Between 70–80 s, two secondary sub-Rayleigh rupture fronts re-rupture the down-dip part of the slab, including spiraling rupture dynamics and initiating backward-propagating rupture fronts (Fig. S6, 170s and 175s). The evolution of the rupture front is shown in the snapshots, with the color scale indicating the slip rate in m/s.

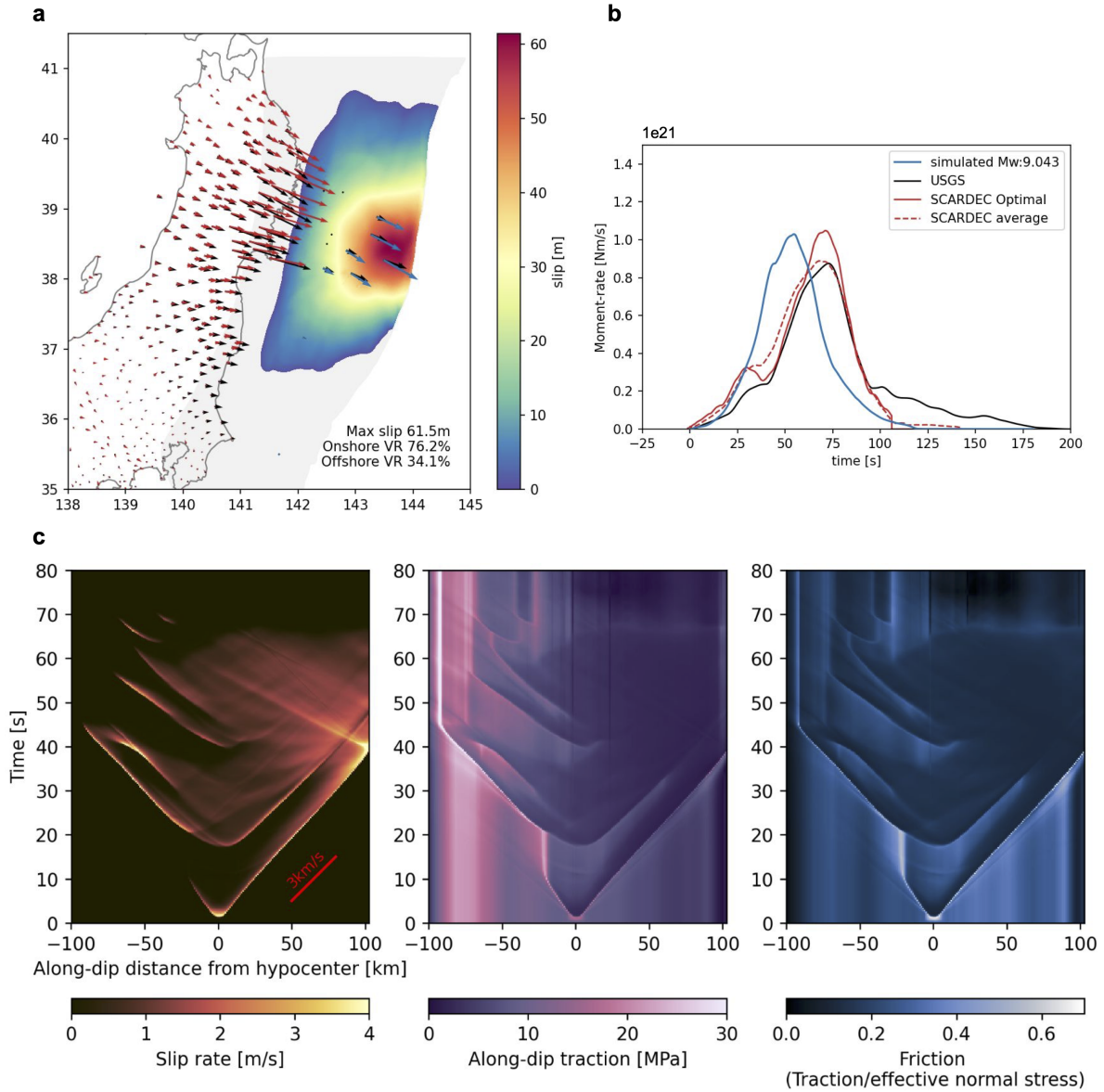


Figure S7: Alternative dynamic rupture model using a uniform weakening distance L of 0.3 m. (a) Fault slip distribution with geodetic data fit. Observed geodetic displacements are shown as black arrows. Onshore and offshore modeled displacements are shown as red and blue arrows, respectively. The model achieves a variance reduction of 76.2 % (onshore) and 34.1 % (offshore). (b) Comparison of modeled moment-rate function and moment-rate estimates from USGS [40] and SCARDEC [41]. (c) Temporal evolution of slip rate (red), along-dip shear stress (purple), and effective friction coefficient (blue) along the hypocentral dip profile, highlighting rapid variations coincident with dynamic rupture reactivation. This model features downdip pulse-like rupture and updip crack-like rupture characteristics.

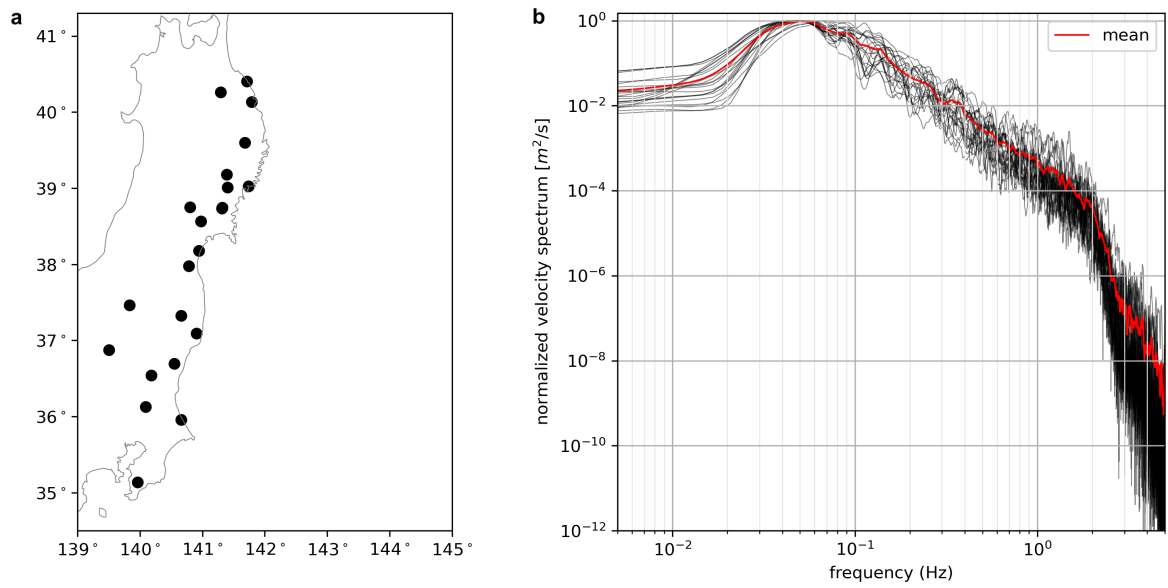


Figure S8: Velocity spectra of modeled waveforms at onshore strong-motion K-net stations. (a) Map showing the K-net seismic station locations. (b) Normalized velocity spectra for all onshore synthetic waveforms (black), with their average spectrum highlighted in red. The average spectrum clearly decays around 2 Hz, indicating the effective maximum frequency resolved by the computational mesh in the simulated seismic wavefield.

References

2. Uchida, N. & Bürgmann, R. A Decade of Lessons Learned from the 2011 Tohoku-Oki Earthquake. *Reviews of Geophysics* **59**, e2020RG000713. doi:10.1029/2020RG000713 (2021).
12. Wong, J. W. C., Fan, W. & Gabriel, A.-A. A Quantitative Comparison and Validation of Finite-Fault Models: The 2011 Tohoku-Oki Earthquake. *Journal of Geophysical Research: Solid Earth* **129**, e2024JB029212. doi:10.1029/2024JB029212 (2024).
35. Ulrich, T., Gabriel, A.-A. & Madden, E. H. Stress, Rigidity and Sediment Strength Control Megathrust Earthquake and Tsunami Dynamics. *Nature Geoscience* **15**, 67–73. doi:10.1038/s41561-021-00863-5 (2022).
39. Brown, L., Wang, K. & Sun, T. Static Stress Drop in the M_w 9 Tohoku-oki Earthquake: Heterogeneous Distribution and Low Average Value. *Geophysical Research Letters* **42**. doi:10.1002/2015GL066361 (2015).
40. Hayes, G. P. Rapid Source Characterization of the 2011 M_w 9.0 off the Pacific Coast of Tohoku Earthquake. *Earth, Planets and Space* **63**, 529–534. doi:10.5047/eps.2011.05.012 (2011).
41. VallÃ, M. A New Database of Source Time Functions (STFs) Extracted from the SCARDEC Method. *Physics of the Earth and Planetary Interiors* (2016).
74. Harris, R. A. *et al.* A Suite of Exercises for Verifying Dynamic Earthquake Rupture Codes. *Seismological Research Letters* **89**, 1146–1162. doi:10.1785/0220170222 (2018).
76. Breuer, A. & Heinecke, A. *Next-Generation Local Time Stepping for the ADER-DG Finite Element Method* in 2022 IEEE International Parallel and Distributed Processing Symposium (IPDPS) (IEEE, Lyon, France, 2022), 402–413. doi:10.1109/IPDPS53621.2022.00046.
80. Fukuyama, E. Automated seismic moment tensor determination by using on-line broadband seismic waveforms [in Japanese with English abstract]. *J. Seismol. Soc. Jpn.* **51**, 149 (1998).
81. Day, S. M., Dalguer, L. A., Lapusta, N. & Liu, Y. Comparison of Finite Difference and Boundary Integral Solutions to Three-Dimensional Spontaneous Rupture. *Journal of Geophysical Research: Solid Earth* **110**. doi:10.1029/2005JB003813 (2005).
109. Wollherr, S., Gabriel, A.-A. & Uphoff, C. Off-Fault Plasticity in Three-Dimensional Dynamic Rupture Simulations Using a Modal Discontinuous Galerkin Method on Unstructured Meshes: Implementation, Verification and Application. *Geophysical Journal International* **214**, 1556–1584. doi:10.1093/gji/ggy213 (2018).

137. Gabriel, A.-A., Garagash, D. I., Palgunadi, K. H. & Mai, P. M. Fault Size–Dependent Fracture Energy Explains Multiscale Seismicity and Cascading Earthquakes. *Science* **385**, eadj9587. doi:10.1126/science.adj9587 (2024).
145. Käser, M. & Dumbser, M. An Arbitrary High-Order Discontinuous Galerkin Method for Elastic Waves on Unstructured Meshes — I. The Two-Dimensional Isotropic Case with External Source Terms. *Geophysical Journal International* **166**, 855–877. doi:10.1111/j.1365-246X.2006.03051.x (2006).
146. Lay, T., Ammon, C. J., Kanamori, H., Xue, L. & Kim, M. J. Possible Large Near-Trench Slip during the 2011 M_w 9.0 off the Pacific Coast of Tohoku Earthquake. *Earth, Planets and Space* **63**, 687–692. doi:10.5047/eps.2011.05.033 (2011).
147. Ide, S. Estimation of Radiated Energy of Finite-Source Earthquake Models. *Bulletin of the Seismological Society of America* **92**, 2994–3005. doi:10.1785/0120020028 (2002).
148. Aochi, H. & Ide, S. Conceptual Multi-Scale Dynamic Rupture Model for the 2011 off the Pacific Coast of Tohoku Earthquake. *Earth, Planets and Space* **63**, 761–765. doi:10.5047/eps.2011.05.008 (2011).
149. Lay, T. A Review of the Rupture Characteristics of the 2011 Tohoku-oki Mw 9.1 Earthquake. *Tectonophysics* **733**, 4–36. doi:10.1016/j.tecto.2017.09.022 (2018).
150. Wang, K. *et al.* Learning from Crustal Deformation Associated with the M9 2011 Tohoku-oki Earthquake. *Geosphere* **14**, 552–571. doi:10.1130/GES01531.1 (2018).
151. Andrews, D. J. Rupture Velocity of Plane Strain Shear Cracks. *Journal of Geophysical Research* **81**, 5679–5687. doi:10.1029/JB081i032p05679 (1976).
152. Hu, F., Oglesby, D. D. & Chen, X. The Sustainability of Free-Surface-Induced Supershear Rupture on Strike-Slip Faults. *Geophysical Research Letters* **46**, 9537–9543. doi:10.1029/2019GL084318 (2019).